

*Approved for public release; distribution is unlimited.*

# **Electric Field Floats in the North Atlantic Current: Validation and Observations**

by Zoltan B. Szuts

Technical Report  
**APL-UW TR 0405**  
June 2004



**Applied Physics Laboratory University of Washington**  
1013 NE 40th Street      Seattle, Washington 98105-6698

Electric Field Floats in the North Atlantic Current:  
Validation and Observations

Zoltan B. Szuts

A thesis submitted in partial fulfillment  
of the requirements for the degree of

Master of Science

University of Washington

2004

Program Authorized to Offer Degree: Oceanography

University of Washington  
Graduate School

This is to certify that I have examined this copy of a master's thesis by

Zoltan B. Szuts

and have found that it is complete and satisfactory in all respects,  
and that any and all revisions required by the final  
examining committee have been made.

Committee Members:

---

Thomas B. Sanford

---

Eric A. D'Asaro

---

Ren-Chieh Lien

---

Jeffrey D. Parsons

Date: \_\_\_\_\_

In presenting this thesis in partial fulfillment of the requirements for a Master's degree at the University of Washington, I agree that the Library shall make its copies freely available for inspection. I further agree that extensive copying of this thesis is allowable only for scholarly purposes, consistent with "fair use" as prescribed in the U.S. Copyright Law. Any other reproduction for any purpose or by any means shall not be allowed without my written permission.

Signature\_\_\_\_\_

Date\_\_\_\_\_

University of Washington

Abstract

Electric Field Floats in the North Atlantic Current:  
Validation and Observations

by Zoltan B. Szuts

Chair of Supervisory Committee:  
Professor Thomas B. Sanford  
Oceanography

Electric field floats (EFF) were designed and built to measure depth-averaged velocity. They were made from commercial RAFOS floats modified to make horizontal electric field measurements through the addition of two pairs of electrodes, electrode arms, rotation vanes, a compass, amplifiers, and a microprocessor. The added second system coordinated its activities with the RAFOS system by an optical serial connection. The electric field observations were combined with RAFOS-derived velocities to form conductivity-weighted depth-averaged velocities ( $\bar{u}^*$ ), which are close to the depth-averaged or barotropic velocity ( $\bar{u}$ ). Two factors relate  $\bar{u}^*$  to  $\bar{u}$ : baroclinic covariance in the vertical between electrical conductivity and velocity, and the ratio of bottom sediment electrical conductance to water column conductance. These were calculated and applied to obtain  $\bar{u}$ .

Four EFFs were deployed in the North Atlantic Current (NAC) in the fall of 1994. They were launched in an eastward flowing branch of the current and were carried through numerous eddies during their 40-day deployments. Hydrographic data collected after deployment permits validation of the electromagnetic method and estimation of the factors relating  $\bar{u}^*$  to  $\bar{u}$ .

An error analysis and comparisons of measurements made by pairs of floats show that the uncertainty in the measured  $\bar{u}^*$  is a few  $\text{cm s}^{-1}$ . Absolute geostrophic velocities were

computed from the hydrographic data using the float velocities as references. Regression analysis indicates that  $\bar{u}^*$  is linearly dependent on the vertically averaged absolute geostrophic velocity ( $r=0.96$ ), as expected from the theory. The baroclinic conductivity-velocity covariance normalized by the vertically-averaged electrical conductivity is  $< 2 \text{ cm s}^{-1}$ , and the fractional bottom conductance is  $0.22 \pm 0.10$ , consistent with previous observations and numerical models. Assuming baroclinic effects to be negligible for the strong signals seen, the observed relation between  $\bar{u}^*$  and  $\bar{u}$  is thus  $1.22 \bar{u}^* = \bar{u}_{\text{est}}$ , where  $\bar{u}_{\text{est}}$  is the estimated barotropic velocity.

Peak  $\bar{u}_{\text{est}}$  speeds of  $0.6\text{--}0.9 \text{ m s}^{-1}$  were observed in an eastward flowing jet, as were speeds of  $0.25\text{--}0.35 \text{ m s}^{-1}$  in nearby eddies. As expected from previous studies, the least energetic flows were observed in regions of weak structure and of entrainment/detrainment of fluid from the NAC, with barotropic velocities of order  $0.1 \text{ m s}^{-1}$ . Baroclinic velocities were larger than barotropic velocities near the surface, with barotropic velocities dominating at 900 m. Integral Lagrangian time-scales for  $\bar{u}^*$  are 1.3–1.6 days, with corresponding length-scales of 15–30 km. The barotropic time and length scales are slightly smaller than those for RAFOS velocities calculated with this data or by Zhang et al. (2001). Transport is estimated for the strong eastward branch of the NAC using spatial scales taken from the literature: a width of 100 km and a triangular velocity cross-section. With a peak speed for  $\bar{u}_{\text{est}}$  of  $0.6 \text{ m s}^{-1}$ , a value that was consistently observed by all floats, the transport is 140 Sv, in agreement with previous results based on absolute velocities.

## TABLE OF CONTENTS

<b>List of Figures</b>	iii
<b>List of Tables</b>	iv
<b>Chapter 1: Introduction</b>	1
<b>Chapter 2: Electric Field Floats</b>	7
2.1 Theory . . . . .	7
2.2 Design and Engineering . . . . .	10
2.3 Previous Trials . . . . .	16
<b>Chapter 3: North Atlantic Current Deployment</b>	18
3.1 Deployment . . . . .	18
3.2 Methods . . . . .	21
3.3 Results . . . . .	24
3.4 Concurrent Data Sets . . . . .	39
<b>Chapter 4: Validation of Data</b>	41
4.1 Error Analysis . . . . .	41
4.1.1 RAFOS System . . . . .	41
4.1.2 EF System . . . . .	43
4.1.3 Combined Error . . . . .	44
4.2 Comparison to URI floats . . . . .	44
4.3 EFF Intercomparisons . . . . .	46
4.4 Comparisons to Absolute Geostrophic Velocities . . . . .	52

4.5	Comparison to PIES/GEM Velocities . . . . .	55
<b>Chapter 5:</b>	<b>Discussion</b>	<b>57</b>
5.1	Observations . . . . .	57
5.1.1	Velocity Spectra . . . . .	59
5.2	Calibration Factors . . . . .	62
5.2.1	Velocity-Conductivity Covariance . . . . .	62
5.2.2	Bottom Sediment Conductance . . . . .	64
5.2.3	Non-Local Currents . . . . .	65
5.3	Dynamics . . . . .	67
5.3.1	Integral Scales . . . . .	67
5.3.2	Transport . . . . .	68
<b>Chapter 6:</b>	<b>Summary</b>	<b>70</b>
<b>Bibliography</b>		<b>73</b>

## LIST OF FIGURES

1.1	Mean currents in the western North Atlantic	2
2.1	The Electric Field Float	11
2.2	EF system block diagram	14
3.1	Chart of the study area	19
3.2	Time series of raw data, float 7	26
3.3	Time series of raw data, float 8	28
3.4	Time series of raw data, float 9	30
3.5	Time series of raw data, float 10	32
3.6	Velocities of all EFFs	34
3.7	Trajectories of all EFFs	36
3.8	Locations of additional data	40
4.1	EFF 7 and URI RAFOS trajectories	45
4.2	EFF 10 and URI RAFOS trajectories	46
4.3	rms $\Delta\bar{u}^*$ between two EFFs versus separation in distance and in time	48
4.4	EFF data compared to absolute geostrophic velocities	53
5.1	Velocity and pressure spectra	61
5.2	Velocity-conductivity covariance	63
5.3	Magnetic field K-index and the standard deviation of $u_{\text{EF}}$	66
5.4	Autocorrelation sequence of $\bar{u}^*$ and its cumulative integral	68

## LIST OF TABLES

2.1	EFF sensor resolution . . . . .	15
3.1	Sound Source Locations and Transmission Times . . . . .	20
3.2	EFF launch information . . . . .	20
4.1	EFF and PIES/GEM velocity comparison . . . . .	56

## ACKNOWLEDGMENTS

I owe a large part of my current position to the support of Tom. Not only did he give me the opportunity to do research in this field before I had started considering graduate school, on this very project in fact, but when I decided to apply to the program he fully supported the round-about route I took. This gradual start has been a wonderful way to begin my graduate studies. His support has not waned since then, and the breadth of opportunities he has given me has expanded my education far beyond the purveys of the program. I am very happy to acknowledge his prior and continuing role in my studies.

Eric D'Asaro, Ren-Chieh Lien, and Jeff Parsons, my committee members, have been excellent sources of enthusiasm and guidance. Their numerous inputs have greatly strengthened this project, and their guidance of my research continues to open my eyes to the broad range of paths and questions that I must confront in my graduate career and beyond.

I am also grateful to Kathleen for understanding and tolerating me over the course of this work, and for most importantly making me keep everything in perspective.

While completing this work I was funded by a National Defense Science and Engineering Fellowship sponsored by the Department of Defense.



## Chapter 1

### INTRODUCTION

This study presents observations of near-barotropic velocities from a subsurface float called an Electric Field Float (EFF). Depth-averaged absolute velocities are derived from oceanic electric fields and RAFOS tracking. The velocity calculated is close to the barotropic velocity, which I define in this paper as the vertical average of the absolute velocity profile. These results add to the few observations of the absolute velocity field in this region, which in turn are directly related to transport. The Lagrangian time series obtained by the floats provides further details of the temporal and spatial variability in the region. This chapter presents previous studies of the North Atlantic Current (NAC) to give context for the results that follow.

The North Atlantic Current has long been recognized as an important and complicated part of North Atlantic circulation. By carrying the waters of the Gulf Stream farther north it links the subtropical and the subpolar regions of the meridional overturning circulation. The highly energetic flow, however, creates large variability that complicates the interpretation of observations.

A strong thermohaline front associated with the NAC separates cold and fresh Labrador Sea water on the continental shelf from warmer and saltier water of subtropical origins in the Newfoundland Basin. A schematic of the NAC, surrounding currents, and topographical features is shown in Figure 1.1. When the Gulf Stream reaches the Southeast Newfoundland Rise at 40°N it bifurcates; a broad and weak current flows east as the Azores Current, while the NAC bends around the ridge and continues north following the 4000 m isobath. The Labrador Current makes a sharp turn at the tail of the Grand Banks and joins the NAC on its inshore edge. At the northern edge of the Newfoundland Basin

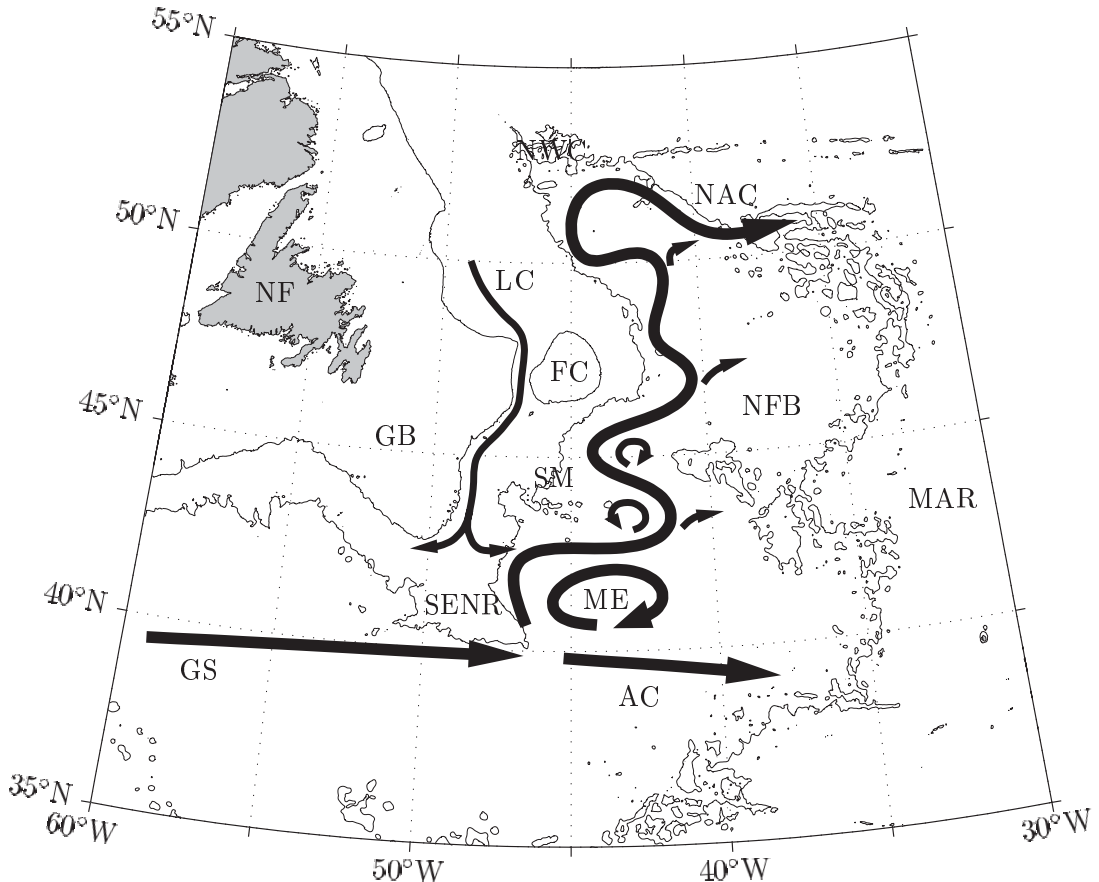


Figure 1.1: Mean current positions in the western North Atlantic. The 500 and 4000 m isobaths are shown (Smith and Sandwell, 1997). The schematics of the Currents are adapted from Rossby (1996) and Meinen (2001). Current names and topographic features are: GS, Gulf Stream; NAC, North Atlantic Current; AC, Azores Current; ME, Mann Eddy; LC, Labrador Current; NWC, Northwest Corner; NF, Newfoundland; GB, Grand Banks; FC, Flemish Cap; SENR, Southeast Newfoundland Rise; SM, Newfoundland Seamounts; NFB, Newfoundland Basin; MAR, Middle-Atlantic Ridge.

the NAC turns sharply and becomes a more diffuse flow to the east and north associated with the weaker subpolar front.

Along its length the NAC forms large meanders that are highly variable in time. Unlike the Gulf Stream, however, the phase of the meanders do not propagate, instead it is the amplitude of the meanders and the location of the axis that vary. The stationary meanders form eddies that usually occur at certain locations, though dependent on the exact location and strength of the NAC. An eddy located at  $41^{\circ}\text{N}$   $44^{\circ}\text{W}$  is the only one that is always present and is called the Mann Eddy after its first observer (Mann, 1967). It moves in relation to the NAC axis (Meinen, 2001); most of the time it is joined with the NAC, but sometimes it is distinct. Other large eddies are persistent but not permanent on either side of the current, and filaments and jets coming off of the NAC can occur on the offshore side (Clarke et al., 1980; Rossby, 1996). Studies based on subsurface drifters (Carr and Rossby, 2001) show that the regions of sharp curvature have high probabilities of water parcel loss from the main current, as shown in Figure 1.1. The exchange of water across the front is small but predominantly in the offshore direction (Dutkiewicz et al., 2001).

The consistent presence of eddies suggest recirculation, not only in the highly localized eddies formed by meanders but also in a broader sense within the Newfoundland Basin for water which is detrained from the NAC. The extent of recirculation has been a major contention, with Worthington (1976) and Schmitz and McCartney (1993) arguing for a separated North Atlantic gyre while Clarke et al. (1980) and Rossby (1996) (among others) describing it as an extension of the Gulf Stream. This argument can be understood as a result of different observational approaches: both basin-wide coverage and fine-scale resolution in time and space cannot be maximized simultaneously. Though recent studies have elucidated certain aspects of the flow, there is still ambiguity on the extent and structure of recirculation.

Many of the historical transport estimates in the region are based on geostrophic calculations. In addition to the above sampling issues the geostrophic velocity profile often has an unknown barotropic offset. With a lack of independent velocity measurements, geostrophic velocities are typically calculated assuming a reference level of no motion deep

in the water column, such as at 2000 dbar or at the bottom, equivalent to assuming that the deep water is stationary. Though the Gulf Stream is confined to the upper ocean when it leaves the continental shelf at Cape Hatteras, by the time it reaches 54°W the deep water has gained momentum and accounts for a large fraction of the transport (Hogg, 1992; Johns et al., 1995). As roughly 60% of the Gulf Stream transport continues as the NAC (Clarke et al., 1980), the NAC may itself have significant transport deep in the water column..

Assuming a level of no motion at the bottom, many investigators (Mann, 1967; Clarke et al., 1980; Krauss et al., 1987, 1990; Schmitz and McCartney, 1993; Meinen and Watts, 2000; Meinen et al., 2000) found the transport of the NAC to vary from 30 to 95 Sv. Many of these observations are along a transect just north of the Southeast Newfoundland Rise and cannot distinguish the recirculating component of the Mann Eddy from the transport of the NAC, although other studies consider basin-scale transects or gyre-scale mass conservation constraints. In 1994 the meander of the NAC just north of the Mann Eddy was particularly strong (Kearns and Rossby, 1998), which may account for the difference between the transport values of Meinen and Watts (2000), Meinen et al. (2000), and others. Two studies estimated the difference of transport between assuming a zero reference velocity at the bottom of the water column and using an absolute reference velocity measured by an independent technique: Meinen et al. (2000) found that the transport is underestimated by 20% with the assumption of a deep level of no motion, compared to a total transport calculated from geostrophic velocities referenced to a POGO transport float; and Meinen and Watts (2000) found a similar underestimate of 30–35%, compared to a total transport calculated from pressure-equipped inverted echo sounder (PIES) data that was calibrated to the observed oceanic variability through gravest empirical modes (GEM). In the northwest corner where the NAC sharply retroflects, measurements from two hydrographic sections yield 40 and 44 Sv when referenced to the bottom (Lazier, 1994)

Absolute transport observations are larger, with magnitudes of 110–145 Sv close to the Mann Eddy. Recent measurements come from Meinen and others:  $112 \pm 23$  Sv (Meinen et al., 2000),  $131 \pm 14$  Sv (Meinen and Watts, 2000), and  $146 \pm 14$  Sv (Meinen, 2001).

Reiniger and Clarke (1975) also found values of 112, 123, and 127 Sv (all  $\pm 50$  Sv). The current meter study in 1982–1983 by Lazier (1994) found transports of 20–120 Sv through a transect in the NW corner, with simultaneous hydrographic (bottom reference level) and current meter transports of 40 and 68 Sv, and 44 and 88 Sv. These are relative errors of 40–50% from assuming a zero reference velocity.

The many transports vary greatly, even after one accounts for assuming the deep water motionless — this appears to be as much a function of the state of the NAC (the amplitude of meanders or the location of the Mann Eddy) and of the location of the measurements as it is a function of the technique used.

Transport estimates from large-scale constraints are much smaller than these direct and time-specific observations. The above points may perhaps account for the large difference between the estimates of Worthington (1976) or Schmitz and McCartney (1993) from direct calculations. Once leaving the strong boundary current of the NAC, water either flows east and north across the Mid-Atlantic Ridge and toward the northern seas, or recirculates in the Newfoundland Basin. Estimates of the through flow due to overturning circulation are about 15 Sv, and roughly 20–25 Sv crosses the Mid-Atlantic Ridge north of the Azores. As there are still large inconsistencies when considering the transport of the separate components as a whole all aspects of the circulation are clearly not fully understood.

Before I can present observations of spatially-averaged barotropic velocities that provide another perspective on the NAC, however, I need to address the electrical characteristics of the region which will influence the measurements of the EFFs.

Though the electrical conductivity of the ocean dominates the generation of electric fields, with conductivity varying up to 50% vertically in the water column, the bottom sediment can also be moderately conductive. The former, as part of the observed oceanic variability, is discussed elsewhere (sections 4.4 and 5.2.1). For the latter, the thickness of the sediment is the most important factor for the total sediment conductance, because the underlying mantle has a very low electrical conductivity and effectively insulates ocean electric fields from the highly conductive core. Over the Mid-Atlantic Ridge the sediment-

tary cover is very thin if not non-existent, for this is where new mantle forms. Sediment thickness increases with distance from the Mid-Atlantic Ridge, as there is more time on geological scales for sediment to accumulate, and is the largest on the continental shelf as a result of continental sediment sources. At the continental slope off of the Grand Banks and Flemish Cap the sediment layers are a few kilometers thick, with localized maxima of 6-7 km (Tucholke, 1986). Despite the presence of a large conduit of turbidity flows called the North Atlantic Mid-Ocean Channel flowing south along 42°W in the Newfoundland Basin, for our purposes it does not appear to significantly affect the basin-wide sedimentary structure.

Though the relation of electrical conductivity to sediment type is poorly known, for the top layers of sediments it is largely dependent on porosity due to highly conductive sea-water filling these gaps. With increasing depth, porosity decreases due to compaction and temperature rises due to heat input from the earth's core. Other effects, such as mineral-dependent solid-state electrical properties, are assumed to be second order and are not resolved in oceanographic electromagnetic models (Flosadóttir et al., 1997). Further discussion of the bottom sediment conductance is in sections 4.4 and 5.2.2.

To understand why these electrical properties are important to interpreting the EFF's data, a brief overview of the electromagnetic theory is necessary. This is presented in chapter 2, followed by a detailed description of the float. The data that form the basis of this dissertation is introduced in chapter 3 along with the methods of data processing. Additional data sets that will be referenced in later sections are also enumerated. Chapter 4 discusses the errors of measurements and the validity of the theory. The chapter progresses from single instrument errors in an error analysis, to comparisons between different floats, to validation against independent velocity data sets. The discussion and interpretation of the measurements are in chapter 5, wherein are discussed measured velocities, calibration factors, and dynamical quantities. Finally, the results are summarized in chapter 6.

## Chapter 2

# ELECTRIC FIELD FLOATS

### 2.1 Theory

Though the fully three dimensional theory of electromagnetic fields in the ocean is complex (Sanford, 1971; Chave and Luther, 1990, among others), geophysical scaling of oceanic flows simplifies the equations into vertically averaged forms that are suitable for explaining electromagnetic observations.

The energy source, the motional induction of salt ions moving through the earth's magnetic field, generates an electromotive force that drives electric currents ( $\mathbf{J}$ ) and electric fields ( $\mathbf{E}$ ) in the water column as described by Ohm's law:

$$\mathbf{E} = \mathbf{u} \times \mathbf{F} - \mathbf{J}/\sigma \quad (2.1)$$

where  $\sigma(z)$  is the electrical conductivity of seawater and  $\mathbf{F}$  is the earth's magnetic field. Self-inductive effects are of order  $1 \times 10^{-9}$  or smaller compared with other oceanographic processes (Sanford, 1971; Tyler et al., 1997), so the velocity  $\mathbf{u}$  can be considered the sole driving force of  $\mathbf{E}$  and  $\mathbf{J}$ . Vertical variations in  $\mathbf{u}$  and  $\sigma$  will determine the electrical structure, as will any conductive bottom sediment.

Geophysical scaling states that the breadth of ocean currents is much larger than their depth,  $L \gg H$ , and correspondingly that the vertical velocity is small compared to the horizontal velocities. This is similar to assuming that the electric currents  $\mathbf{J}$  circulate in a vertical plane. In this situation  $\mathbf{J}$  arises from the local velocity field throughout the water column and within a radius of a few times the water depth  $H$  (Chave and Luther, 1990). Any horizontally-circulating electric currents that may be present can be thought of as non-local currents  $\mathbf{J}^*$ , which are generated by bottom topography, meandering ocean currents, magnetotelluric storms, and gradients of conductance transport (Sanford, 1971;

Tyler et al., 1997).

Applying the geophysical assumption results in the electric field being predominately horizontal ( $\mathbf{E}_h$ ) and only dependent on the horizontal velocity ( $\mathbf{u}_h$ ) and the vertical component of the earth's magnetic field ( $F_z$ ). The electric field is uniform vertically in the water column, which has been demonstrated both theoretically (Longuet-Higgins et al., 1954; Sanford and Flick, 1975) and observationally (Sanford et al., 1978; Luther et al., 1991). Vertically averaging the right-hand side of equation 2.1 yields

$$\mathbf{E}_h = \bar{\mathbf{u}}^* \times \hat{\mathbf{z}} F_z \quad . \quad (2.2)$$

The velocity  $\bar{\mathbf{u}}^*$  corresponds to a vertical integral of the conductivity and velocity structure of the water column, extending from the bottom of any conductive sediment layers to the top of the water column, divided by the mean conductivity and the mean velocity (see equation 2.4). The electric current integrates to zero because it is closed in the vertical plane, at least to the degree that the non-local currents are insignificant. The magnitude of  $\mathbf{J}^*$  will be assumed small; theory, observations, and modeling have shown this to be accurate in most situations. This assumption is discussed in greater detail in sections 4.4 and 5.2.3.

The last modification necessary to this theory adjusts for measurements taken from a moving platform

$$\mathbf{E}_h = (\bar{\mathbf{u}}^* - \mathbf{u}_{\text{instr}}) \times F_z \hat{\mathbf{z}} = -\mathbf{u}_{\text{EF}} \times F_z \hat{\mathbf{z}} \quad (2.3)$$

From a Lagrangian platform the observed  $\mathbf{E}_h$  corresponds to the relative velocity between the float and  $\bar{\mathbf{u}}^*$  (i.e.  $\mathbf{u}_{\text{instr}} - \bar{\mathbf{u}}^*$ ), which we call the electric field velocity  $\mathbf{u}_{\text{EF}}$ . Similar to how motional induction of saltwater generates an electric field, the movement of the sensor through the earth's magnetic field will generate an equivalent electric field. The float velocity ( $\mathbf{u}_{\text{instr}}$ ) is calculated from a separate system (RAFOS tracking, notated  $\mathbf{u}_{\text{RAFOS}}$ ), from which calculation of  $\bar{\mathbf{u}}^*$  is trivial.

Though the float measures  $\bar{\mathbf{u}}^*$ , this is closely related to the true barotropic velocity by

$$\bar{\mathbf{u}}^* = \frac{\int_{-H_s}^0 \sigma \mathbf{u} \, dz}{\int_{-H_s}^0 \sigma \, dz} = \left( \frac{1 + \gamma}{1 + \lambda} \right) \bar{\mathbf{u}}. \quad (2.4)$$

Here  $\bar{\mathbf{u}}$  is the barotropic velocity:

$$\bar{\mathbf{u}} = \frac{1}{H} \int_{-H}^0 \mathbf{u} \, dz,$$

$\gamma$  is the normalized conductivity-velocity covariance:

$$\gamma = \frac{\overline{\sigma' \mathbf{u}'}}{\overline{\sigma' \mathbf{u}}}, \quad \text{with} \quad \overline{\sigma' \mathbf{u}'} \equiv \frac{1}{H} \int_{-H}^0 \sigma' \mathbf{u}' \, dz,$$

$\lambda$  is the ratio of the sediment conductance to the oceanic conductance:

$$\lambda = \int_{-H_s}^{-H} \sigma \, dz \Big/ \int_{-H}^0 \sigma \, dz,$$

$H$  is the depth of the water column, and  $H_s$  is the bottom of the conducting sediment. The first equality in equation 2.4 explicitly shows the vertically averaging of  $\bar{\mathbf{u}}^*$ , where the integration goes from the bottom of conducting sediments to the top of the water column. The physics of this description is more easily seen in the second equality, however, where I have performed a Reynolds decomposition in the vertical (i.e.  $f(z) = \bar{f} + f'(z)$ ) on  $\mathbf{u}$  and  $\sigma$  and divided both numerator and denominator by  $\bar{\sigma}H$ .

Two factors relate  $\bar{\mathbf{u}}^*$  to  $\bar{\mathbf{u}}$ : the first  $\gamma$  is due to covariances in the vertical between  $\mathbf{u}$  and  $\sigma$ , a baroclinic phenomena; and the second  $\lambda$  is due to conductive sediment that shorts the oceanic electric field and diminishes  $\bar{\mathbf{u}}^*$  relative to  $\bar{\mathbf{u}}$ . In currents that are surface intensified like the NAC,  $\gamma$  can be expected to be non-zero. The ratio of sediment conductance to water column conductance ( $\lambda$ ) has been shown to be small (0–0.2) both in models (Chave and Luther, 1990; Flosadóttir et al., 1997; Tyler et al., 1997) and in observations (Sanford et al., 1985; Sanford, 1986; Chave and Luther, 1990). Both terms are discussed in more detail in sections 4.4 and 5.2

## 2.2 Design and Engineering

The EFF is a commercial RAFOS float (Bathy Systems, Inc) equipped to measure 2-D horizontal electric field measurements. RAFOS floats are expendable subsurface floats whose mission scheme is to sink to a predetermined depth or isopycnal for a set period of time, record acoustic signals used for tracking, and then rise to the surface when finished. Once at the surface it transmits stored data to ARGOS satellites for recovery. The EFF is organized into two separate systems that can communicate with each other: the standard RAFOS system, which performs RAFOS tracking and data telemetry, and the electric field (EF) system, which obtains the electric field measurements.

Four modifications have been made to the RAFOS system to allow it to work with a second system. (1) Bathy Systems modified the code to allow serial data communication. These connections are optically isolated to prevent unwanted electric current from polarizing the electrodes in the EF system. One connection is for RAFOS CPU reset, and the other two are for serial communication. (2) Data can be received from the connections and stored in internal RAM for satellite transmission. (3) The pressure and temperature sensors have been removed and transferred onto the EF system to allow a higher sampling rate. (4) A mission termination command can be received causing the RAFOS to jettison the ballast. This is a safety mechanism in case the float descends below a maximum pressure.

The RAFOS system is only powered when it needs to receive the acoustic tracking signal. For the study discussed in the next chapter the sound sources emitted signals every 12 hours with an offset of 30 minutes between sources. The float's listening windows last for 30 minutes for each source; thus with four sources the RAFOS system is on for 2 hours every 12-hour positioning cycle. The arrival time of the signal is determined by correlating the signal received at the hydrophone with a replica of the transmitted waveform. The transmitted signal is about 260 Hz and lasts for 80 seconds during which time the signal frequency is modulated by a linear slide of 1.5 Hz. The internal processing stores the arrival times and the amplitudes for the signals having the two highest correlations.

At the end of the mission the float applies electric current for several minutes to corrode

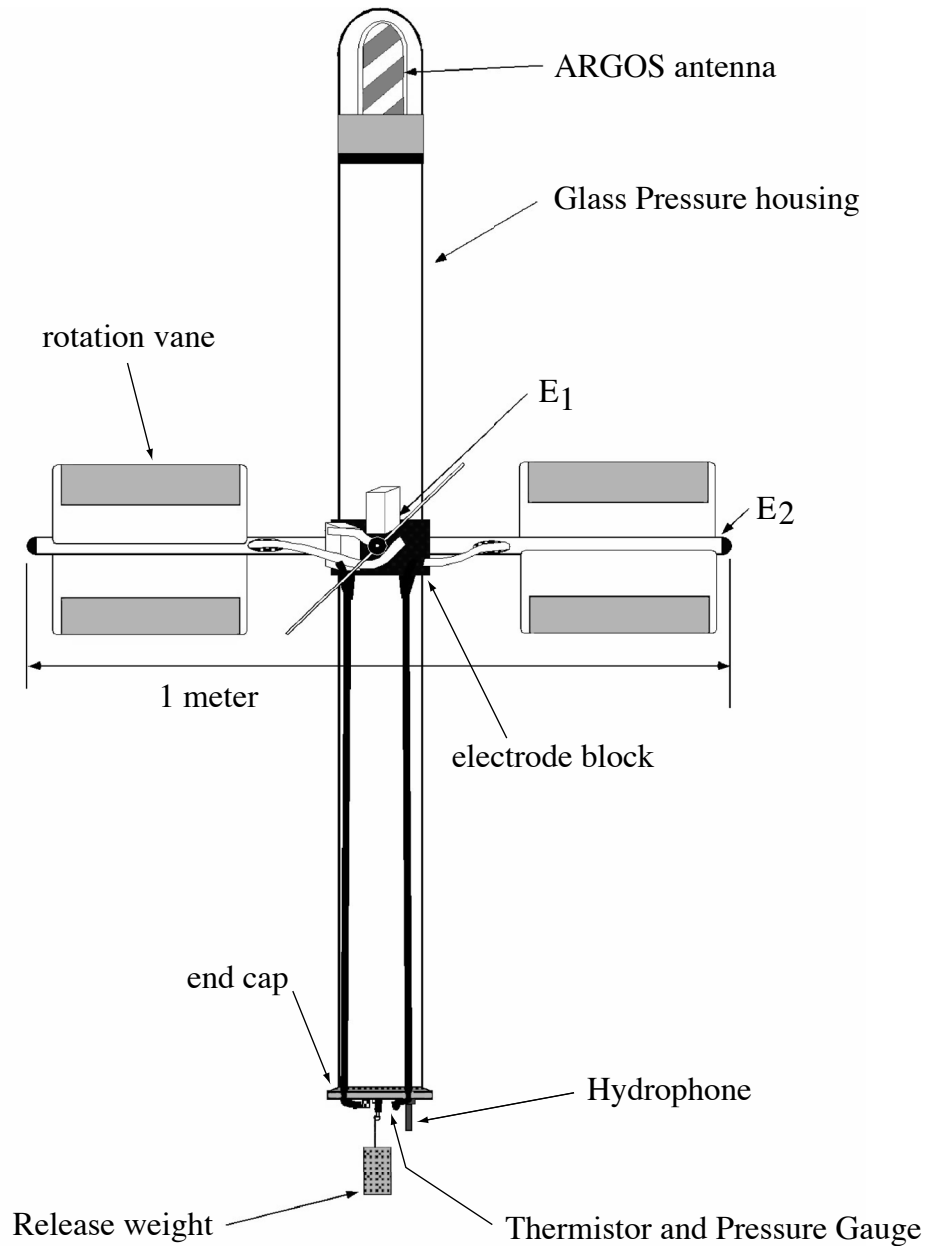


Figure 2.1: The Electric Field Float (EFF). The cylindrical glass housing is the RAFOS float base. Electrode arms (labeled  $E_1$  and  $E_2$ ), an electrode block, rotation vanes, and cables from the electrodes to the end cap, are added externally to allow high quality measurements of the ambient electric field. Inside the pressure housing (not shown in this figure) are a microprocessor, memory, batteries, a fluxgate magnetic compass, and various small electronic components. See the text and Figure 2.2 for more details.

the connection to the ballast weight. After a 30-minute delay to allow the float to reach the surface, it starts transmitting to the ARGOS satellites. EF data are inserted into the RAFOS RAM behind RAFOS data after each transmission. The RAFOS float transmits a 30-byte data packet approximately every 45 seconds. After going through the entire 4000-byte RAM buffer it starts again from the beginning — this way the data are transmitted multiple times to ensure complete reception of all packets. Each week the EFF replaces the contents of the RAFOS buffer with subsequent EF data. The batteries were designed to last 2 months of surface transmission.

The EF system is composed of two pairs of electrodes and their external housing, a gimbaled fluxgate compass, amplifiers, A/D converters, a microprocessor, the RAFOS pressure and temperature sensors, and a battery pack.

The external housing consists of electrode arms, vanes at a 45° angle, and an electrode block that holds the arms onto the RAFOS body (see Figure 2.1). The electrode block is PVC, while the tubes and vanes are Lexan. The other external components are also made of non-conducting materials: either borosilicate glass for the RAFOS body or anodized aluminum for the RAFOS end cap. Electrically inert materials are necessary on the outside because otherwise they would generate localized corrosion currents that would distort the ambient electric field. The electrodes are located in the electrode block and are connected to the ocean at the end of the tubes, giving an effective electrode separation of 1 m. Inside the electrode blocks are pre-amplifiers that increase the signal by a factor of 100 before it enters the float body.

Agar is inserted at the end of the electrode arms to minimize electrode drift and to keep them filled with salt water during deployment. By preventing rapid exchange of the water inside the arms, the agar plugs dampen environmental changes that affect the electrode self-potentials. With a long time constant, environmental changes will occur at longer time-scales and can be more readily removed from the recorded electric field during data processing. The Ag-AgCl electrode technique of Arevalo et al. (1985) was used to get offset voltages of around 100  $\mu$ V. The electrodes were built at the Applied Physics Lab.

Angled vanes are attached to the electrode arms so vertical water velocity will rotate

the float. Though floats with rotation vanes that measure the vertical water velocity have been developed in their own right (for example Voorhis, 1968; Webb and Worthington, 1968; Gascard, 1973; Lherminier, 1998), in the case of the EFF this is strictly necessary to allow accurate removal of the electrode offsets. Large vanes far from the body maximize rotational torque from the weak motions of internal waves, for large-scale vertical velocities are not expected at the desired equilibrium depths. Below the thermocline where the ocean environment varies only slowly and where the electrode offsets should not change rapidly, a few rotations per measurement period are sufficient to remove the time-varying electrode offsets.

Internal waves are the primary source of vertical water motion below the thermocline, though large scale vertical motion can be forced by other processes. The vertical displacement of isopycnals follows the Garrett-Munk hypothesis (Munk, 1981)

$$\langle \zeta^2 \rangle \approx 53 \left( \frac{N}{N_0} \right)^{-1} [\text{m}^2]$$

where  $N$  is the local buoyancy frequency and  $N_0$  is a reference buoyancy frequency set to 3 cycles per hour. At a depth of 2000 m the root-mean-square displacement is about 13 m. At lower stratification the vertical displacement will be larger but of lower frequency, while at higher stratification the opposite will occur. In particular, near the thermocline where internal waves can be generated the strong stratification will result in small vertical displacements despite high energy levels.

A second design concern is how the float will perturb the surrounding electric field. Sanford et al. (1978) treated the case where an electromagnetic instrument takes measurements at a distance away from its body that is large relative to its diameter. The EFF fits this case, since the measurement points are 50 cm away from its 5 cm radius body. Assuming the instrument's shape to be a vertically oriented ellipsoid, there is insignificant distortion of the electric current. Also, any relative horizontal motion between the surrounding water and the instrument will have no effect on the derived velocity. These results are for the general case of a vertically profiling instrument, and will certainly hold in the case of an isobaric float that experiences weak vertical velocities and closely follows horizontal flow.

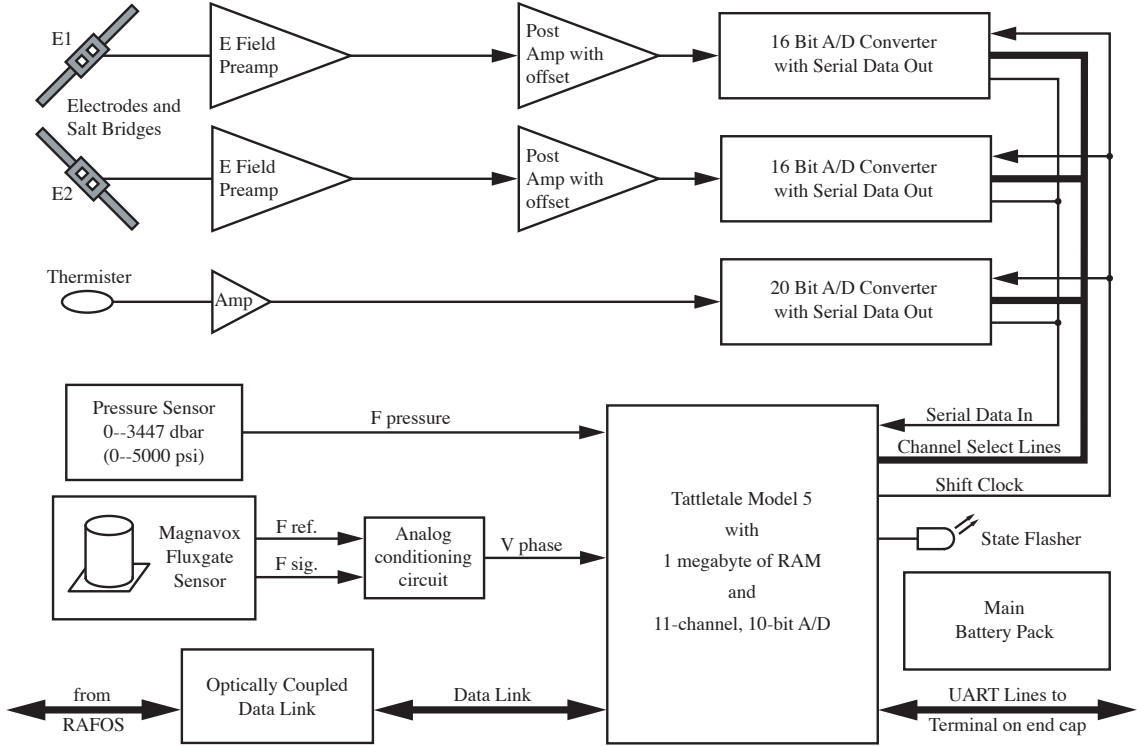


Figure 2.2: A block diagram of the connections among the EF system components, also showing the connection between the EF and the RAFOS systems.

The internal connections of the EF system are shown in Figure 2.2, as are the optically isolated connections with the RAFOS system. The EF processor provides the only source for user input; before deployment the RAFOS mission is initialized through the EF system.

The resolution of the sensors is shown in Table 2.1, as well as their sampling period. The electrode resolution of  $0.153 \mu\text{V}$  is equivalent to a velocity resolution of  $3.3 \text{ mm s}^{-1}$ . The raw data are processed every 4 hours before being saved: temperature and pressure are averaged; electric field measurements come from a least squares fitting procedure; and the heading measurements are combined to give a rotation rate. Because of the different measurement requirements the EF system is awake more often than the RAFOS system.

Every time the compass measurement shows that the float has turned past  $180^\circ$  one of two half turn counters is incremented depending on the direction of rotation. The total

Table 2.1: EFF sensor resolution.

Sensor	Sampling Interval (minutes)	Digital Resolution
electrode pairs (2)	2	$0.153 \mu\text{V}$
compass	2	$1.5^\circ$ (stored) $0.4^\circ$ (internally)
pressure	6	0.1 dbar
temperature	6	$4 \times 10^{-3} \text{ }^\circ\text{C}$

number of half turns in both directions is saved at the end of the 4 hour processing window.

The measured electric potentials are fitted to a 5-term function to obtain the electric field vector. The function is of the form

$$f_i = a_0 + a_1 t_i + a_2 t_i^2 + a_3 \sin \theta_i + a_4 \cos \theta_i + \epsilon_i \quad (2.5)$$

for the  $i$ th measurement, where  $f$  is the measured potential,  $\epsilon$  is the error,  $a_0 \dots a_4$  are unknown coefficients,  $t$  is time, and  $\theta$  is the orientation of the electrode arms relative to magnetic north. The coefficients are determined by a least-squares regression that minimizes the error.

The mean, linear, and quadratic terms remove the electrode self-potential and its linear and quadratic drifts in time. The two components of the electric field in geomagnetic coordinates are given by  $a_3$  and  $a_4$ . This fitting procedure is performed on both electrode arms separately using 120 observations taken over 4 hour intervals, resulting in two independent velocity measurements. Though it would be possible to calculate the 2-D electric field simultaneously from the two pairs of electrodes, failure of either electrode pair would disrupt the electric field measurements.

A measure of the quality of the fit is also calculated, which is related to whether the float rotates through a sufficient range of orientations during the averaging period. The

fitting calculation (equation 2.5) can be expressed more compactly as

$$\mathbf{f} = \mathbf{a} D \quad (2.6)$$

where  $\mathbf{f}$  is a vector of the measured electric potentials of size  $1 \times 120$ ,  $D$  is the matrix of the five basis functions ( $5 \times 120$ , where each basis function  $d_j$  is  $1 \times 120$ ), and  $\mathbf{a}$  contains the coefficients to be determined ( $1 \times 5$ ). The basis functions ( $d_j$ ) are a constant 1,  $t$ ,  $t^2$ ,  $\cos(\theta)$ , and  $\sin(\theta)$ , and a unique solution will exist only if they are independent. For numerical stability the basis functions of time have a zero mean and all basis functions are normalized to unit variance. Taking  $DD^T$  results in a  $5 \times 5$  square matrix whose  $i,j$ th element is the correlation of the  $i$ th and  $j$ th basis functions, which will be between -1 and 1. The maximum value of the off-diagonal elements is called ‘ddt’ and shows the greatest degree of dependence between any of the basis functions. If this is close to one the fitting problem may be ill-conditioned, in which case the solution will have large uncertainties if it exists at all.

### 2.3 Previous Trials

Multiple engineering trials and launches of opportunity were performed in the development of the EFF. The evolution and performance of the float is briefly discussed here.

The first engineering deployment was in November 1990 east of Abaco Island, the Bahamas (Sanford et al., 1993). The goal was to evaluate the stability of the electrodes, the adequacy of the electrode self-potential determination, and the performance of the processing software. The last two goals depended heavily on the rotation of the float, which was less than expected due to the shallow angle ( $15^\circ$ ) of the vanes. The angle was changed to  $45^\circ$  for subsequent experiments.

To test the reliability of rotation with the new blade angles two floats were deployed during the TOGA/COARE experiment in the equatorial Pacific in February 1993. Results were inconclusive because of ballasting difficulties. The first float deployed sank too deep, triggering the EF mission abort signal, and was recovered. The same float was re-ballasted and more conservatively deployed. Weight was added to it by divers as it floated near the

surface, but only enough weight was added to make it sink to the base of the surface mixed layer.

Another deployment of opportunity came when Tom Rossby deployed the NAC sound sources in July 1993. Three floats were prepared for launch during R/V *Oceanus* cruise 259. The towed transport meter, an instrument that measures the component of  $\bar{u}^*$  perpendicular to the ship path, was used during transits to obtain a separate measure of the horizontal electric fields. Two floats were deployed but there were complications in deployment. The first wasn't launched because the tag line snagged during deployment, and the second lost the salt water in the electrode arms and so gained enough buoyancy to prevent it from sinking. ARGOS transmissions from it later confirmed that it remained on the surface. In subsequent deployments the ends of the electrode arms were filled with agar to prevent the water from draining out.

As detailed in Sanford et al. (1995), EFFs were launched off Monterey Bay, CA in the California Current in March 1994. They used sound sources deployed by Curtis Collins and Newell Garfield that transmitted every 8 hours. Two EFFs were deployed, but one appeared to have reset itself and only transmitted default information. The floats were close to each other (75 km) upon surfacing after a 30 day mission. EFF 10 moved vertically only about 25% of the movement of the surrounding water, being more isobaric than isopycnal in response to vertical motion. Evident in the measured velocities were small (1 km) clockwise loops in  $\mathbf{u}_{\text{RAFOS}}$ , as would be expected for inertial and tidal motions. The near-barotropic velocity  $\bar{u}^*$  was stable and small, despite a greater change in  $\mathbf{u}_{\text{RAFOS}}$ , and remained parallel to the large-scale topography as expected for barotropic flow. At a depth of 800 m the average speed of  $3.3 \text{ cm s}^{-1}$  to the NW was composed of  $2 \text{ cm s}^{-1}$  of barotropic flow. All data were received from ARGOS. The success of this deployment gave confidence for a larger trial in the NAC the following fall.

## Chapter 3

### NORTH ATLANTIC CURRENT DEPLOYMENT

#### **3.1 Deployment**

The most extensive deployment of EFFs was performed in the North Atlantic in October 1994. This opportunity took advantage of a cruise to deploy sound sources by Tom Rossby in support of his RAFOS float program. The sound sources transmitted every 12 hours, and their locations are shown in Figure 3.1 with further information in Table 3.1.

Five floats were deployed during CSS *Hudson* cruise 94030; deployment information is listed in Table 3.2. Floats 7 and 10 were deployed along a hydrographic transect within 60 km of each other, at a position seaward of the continental slope near the 4500 m isobath. Floats 8 and 9 were deployed within 50 km of each other but along the next transect to the east. They were initially close to the Newfoundland Seamounds. EFF 6 was deployed close to the tail of the Southeast Newfoundland Rise, but it was launched without a necessary communications dummy plug; nothing was heard from this float after deployment.

The floats were ballasted to sink to 500 m. Additional weight was added with a corrodible link to ensure that any air bubbles would not prevent the float from sinking, but which would release after the float sank to depth. Two floats (7 and 8) released this additional weight 10 hours after launch, while the other two (9 and 10) did not. The difference made floats 9 and 10 equilibrate at about 850 dbar. After field-replacement of a regulator chip, the inert freon initially used to fill the inside of float 8 was replaced with nitrogen, causing this float to equilibrate at a depth of 150 m.

All floats were set to surface on December 9 to transmit the data to ARGOS. The floats transmitted for 2 months, although unfortunately float 10 became quiet after 4 days on the surface.

The initial data transmissions were misdirected and scrambled within the Service Argos

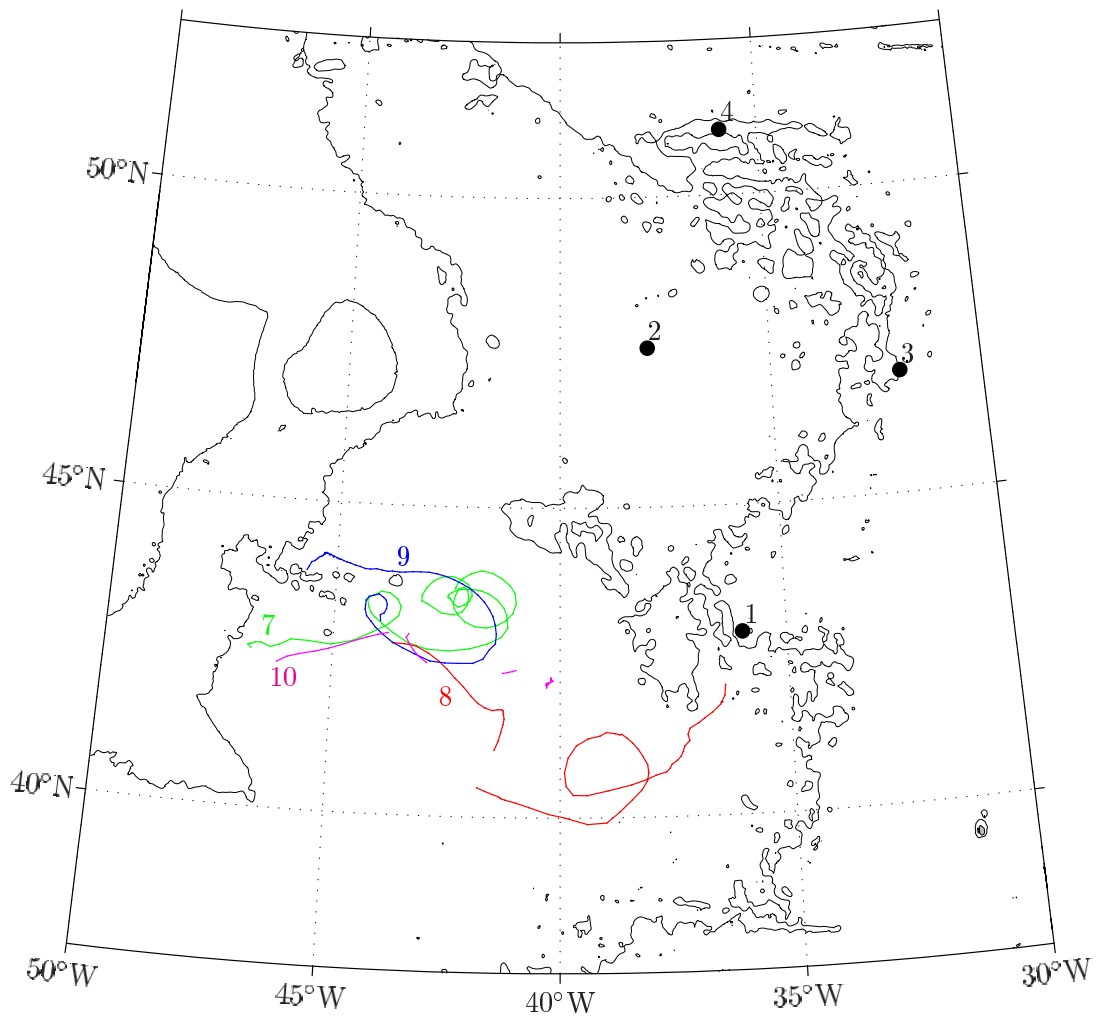


Figure 3.1: Small-scale chart of the study area. The trajectories of the floats are shown by the solid colored lines (green, EFF 7; red, EFF 8; blue, EFF 9; magenta, EFF 10), the sound sources are labeled 1–4, and the 500 and 4000 m isobaths are shown (Smith and Sandwell, 1997).

Table 3.1: Sound Source Locations and Transmission Times. These Sound Sources were deployed by Tom Rossby, were active from 1993-1995, and transmitted every 12 hours. Clock corrections are not shown.

Number	Longitude	Latitude	Emission Times	
	(°N)	(°W)	(GMT)	
1	42.948	35.973	0030	1230
2	47.570	37.915	0100	1300
3	46.968	31.947	0130	1330
4	51.049	35.947	0200	1400

Table 3.2: EFF launch information

Number	Date (1994)	GMT	Latitude	Longitude	Comments
6	Oct 16	7:52	40° 56.92' N	50° 12.09' W	15° C at 200 m
7	Oct 24	0:35	42° 37.69' N	46° 51.15' W	10° C at 450 m
8	Oct 28	7:40	42° 51.51' N	43° 41.83' W	10° C at 700 m
9	Oct 28	0:11	43° 11.93' N	43° 57.67' W	10° C at 500 m
10	Oct 23	18:14	42° 26.25' N	46° 11.17' W	10° C at 650 m

computer system, and no records were kept to document what happened. They corrected the problem 2 weeks after the floats had surfaced. From these later broadcasts John Dunlap backed out as much of the initial data as possible. This was especially important for float 10, for which only scrambled data were available. With decoding an additional 20–30% of data were recovered.

Other complication for data transmission were stormy weather and low surface buoyancy, causing many incomplete packet transmissions. The winds were routinely above 30 knots or higher in the North Atlantic in December 1994, including a few days of 50 knot winds (Meteorological Service of Canada, National Archives and Data Management

Branch, 2002). Presumably waves frequently covered the transmission antennae, reducing the continuity of data reception. The floats had only minimal positive buoyancy at the surface, another factor in the frequency of splash-overs. John Dunlap minimized the loss of data due to incomplete packets by accepting any data bits that were received at least twice.

### 3.2 Methods

The data processing involves two main steps: converting the raw RAFOS data from time of arrival to geographic position fixes, and combining the float velocity with the electric field velocity.

The time of arrival (TOA) of the acoustical signals at the float are adjusted for drifts in the sound source clocks, which were provided by Tom Rossby's group. For each float the TOAs from each sound source are selected by hand to yield a smooth track. Though the float clocks can be corrected with a mean offset and a linear drift obtained from clock offsets at launch and at the time of first satellite transmission (compared with the expected time of first transmission), a hyperbolic tracking scheme was used instead as it is independent of any drifts in the float clock. The difference between TOAs from two sound sources is related to the relative distance between the float and each sound sources, with the offset of the float clock in the first TOA cancelling the same offset in the second TOA. Instead of the lines of position being two circles about the locations of the sound sources, as would be the case using each TOA directly as a range, the difference of TOAs give hyperbolic lines of position in relation to the locations of the sound sources. A constant sound speed was used to convert from time of propagation to distance. Three sound sources were used for tracking: numbers 1, 3, and 4 in Figure 3.1. The reception from sound source 2 was too weak to give reliable data; its emission amplitude was reduced due to a spurious mechanical resonance close to the emission frequency (Anderson-Fontana et al., 1996). With three sound sources, three pairs are formed and three lines of position are calculated. Though, to be exact, each pair of sound sources yields two lines of position, none of the floats cross the centerline between any pairs and thus one of the lines of position can be discarded.

The float's location is overdetermined by one degree of freedom. The effects of Doppler shifts of the acoustic signals are corrected iteratively from initial calculations of the float's location and speed.

The tracking was performed by Kathleen Schulz-Tokos with programs she developed at the University of Rhode Island and the Institut für Meereskunde, Universität Kiel. Gaps in position of 5 or less consecutive sampling periods (equivalent to 2.5 days) were interpolated with cubic spline interpolation. Float velocities  $\mathbf{u}_{\text{RAFOS}}$  were calculated as the centered difference between positions 24 hours apart. With a centered differencing scheme velocities could not be calculated at times adjacent to those with missing positions, but this effect was minimized by the interpolation of position over gaps of less than 3 days. The RAFOS processing techniques were similar to those used by Tom Rossby's group: they were performed by a former member of his group (K. Schulz-Tokos) using analysis programs developed there and using their sound source clock drift data.

The EF variables processed every 4 hours — temperature, pressure, electric field, half turn rotations, and ddt — were binned and averaged onto the times at which RAFOS positions were calculated. The average electric field velocity  $\mathbf{u}_{\text{EF}}$  was calculated by  $\mathbf{u}_{\text{EF}} = \phi_h/(F_z L)$  and combined with  $\mathbf{u}_{\text{RAFOS}}$  to obtain  $\bar{\mathbf{u}}^*$  using equation 2.3, and where  $L$  is the electrode separation. Since Sanford et al. (1993) found that if  $\text{ddt} \leq 0.85$  the calculated velocity from the two electrode pairs had an rms error less than  $1\text{--}2 \text{ cm s}^{-1}$ , any  $\mathbf{u}_{\text{EF}}$  measurements for which ddt was greater than 0.85 were excluded from analysis. Only a few data points were removed with this criterion.

The rotation rate of the float was measured by two values that counted the number of clockwise or counter-clockwise half rotations ( $r_{cw}$  and  $r_{ccw}$ ) during the four hour averaging period. Two important parameters can be formed with these counters: the total number of half turns  $r_{cw} + r_{ccw} = N_r$ , and the total summed half turns  $\sum_{t'=0}^t (r_{cw} - r_{ccw}) = Tr(t)$ . The sum of the counters gives the absolute number of half turns made by the float, which needs to be sufficiently large for the on-board demodulation of the oceanic electric field to be well-conditioned. The sum of the difference is a measure of how much bulk water flows past the float. It is expected that isopycnal oscillations due to internal waves would

provide a steady source of rotation for the float, but such motions would result in no mean displacement of water relative to the float. Any non-zero integrated water motion past the float can be interpreted as vertical water motion. Vertical current meters have been designed to measure the vertical velocity of water in just this fashion (e.g. Voorhis, 1968; Webb and Worthington, 1968; Gascard, 1973).

Though the conversion from rotation rate to vertical water motion past the float is most accurately performed using a transfer function that depends on frequency (Voorhis, 1968, 1971), rotation data averaged over 4 hours will not resolve high frequency motion. Under the assumption that the float rotates at a constant rate, the vertical water displacement relative to the float ( $P$ , in meters, for a full rotation) is

$$P = \frac{\lambda}{2} + \sqrt{\frac{\lambda^2}{4} + \frac{\Gamma^2}{\tau |\Omega|}}$$

where  $\lambda$  and  $\Gamma$  are characteristic dimensions of the float,  $\Omega$  is the rotation rate of the float, and  $\tau$  is a steady rotation damping time (Voorhis, 1971). They are defined as

$$\begin{aligned} \lambda &= \frac{4\pi}{3} \left( \frac{r_1^3 - r_0^3}{r_1^2 - r_0^2} \right) \tan \alpha \\ \Gamma &= \sqrt{\frac{4\pi I_f}{\rho C_L n R_b A_b \cos \alpha}} \\ \tau &= \frac{r_g^2}{4\mu} \end{aligned}$$

where  $r_1$  and  $r_0$  are the outer and inner radii of the blades, respectively,  $\alpha$  is the angle the blades make with the horizontal,  $I_f$  is the rotational moment of inertia of the float around the vertical axis ( $= mr_g^2$ ),  $\rho$  is the density of sea water,  $C_L$  is the coefficient of lift of the blades ( $= 0.1$ ),  $n$  is the number of blades,  $R_b$  is the average radius of the blades,  $A_b$  is the area of a blade,  $r_g$  is the radius of gyration, and  $\mu$  is the viscosity of water. The coefficient of lift is assumed small because of the pipe strut across the blade that disrupts flow and the low Reynolds number of these motions (Sanford et al., 1993). At rotation rates of greater than 6 rotations per 4 hour period the value for  $P$  is nearly constant at 2.18 m per rotation. Total rotation rates of 5 half-turns per averaging period were consistently observed by the EFFs with only a few exceptions. As vertical water motions are expected

to be neither energetic nor of primary interest, a simple scale factor between rotation and vertical water motion shall be assumed here. In particular, vertical displacement of water past the float are given by  $Z_r = T_r * P/2$ ,  $P/2 = 1.09$  m per half rotation.

### 3.3 Results

The EFFs recorded data for about 45 days, though many gaps arose from the unfavorable weather after surfacing and the complications at Service Argos. The time series of physical variables are shown in Figures 3.2–3.5, and the float tracks are shown in Figures 3.7 and 3.6. The time series are broken up into RAFOS (Figures 3.2–3.5a–d) and EF (Figures 3.2–3.5e–h) data streams, which have sampling intervals of 12 and 4 hours, respectively. As the RAFOS fixes occur every twelve hours,  $\bar{u}^*$  can only be calculated at the same frequency. All velocities calculated ( $\mathbf{u}_{\text{RAFOS}}$ ,  $\mathbf{u}_{\text{EF}}$ ,  $\bar{u}^*$ ) are shown in terms of their u and v components and their speed. The ratio of baroclinic velocity to barotropic velocity is approximated as  $|\mathbf{u}_{\text{EF}}|/|\bar{u}^*|$ , which gives an indication of the dominant velocity component. Pressure, temperature, rotations, and ddt were recorded every 4 hours by the EF system and are shown in these figures.

All floats were deployed in an eastward flowing branch of the NAC. A few synoptic features of the flow are observed in multiple trajectories, for instance a meso-scale eddy located at 43.25°N 44°W, fast currents at 42.5°N 45°W and 42.5°N 43°W, and a meander of the NAC at 41°W. Due to small spatial and temporal scales the floats enter and exit these regions at different times and locations.

Floats 7 and 10 were deployed together just offshore of the 4000 m isobath. Hydrographic data taken at launch shows that float 7 was close to the axis of the NAC, whereas float 10 was 50 km seaward. My definition of the axis of the NAC is where the 10°C isotherm is at a depth of 450 m, the same as that used by Meinen (2001). This is the location where the velocity in stream coordinates has a surface maximum. At a depth of 1000 m the velocity maximum broadens and shifts seaward by 50 km. The launch positions of the floats relative to the current axis can explain their later behavior. Float 7 was carried further by the current because it started close to the center of the current, whereas float

10 left the current earlier on the same side where it was launched.

Float 7 was in initially weak current at a depth of 500 m. In its first three days both  $u_{\text{RAFOS}}$  and  $\bar{u}^*$  were less than  $0.3 \text{ m s}^{-1}$  and varied often in direction. It became entrained in a fast eastward branch of the NAC with a maximum  $u_{\text{RAFOS}}$  of  $0.92 \text{ m s}^{-1}$  and  $\bar{u}^*$  of  $0.44 \text{ m s}^{-1}$ . An eddy north of the mean NAC position carried the float fully around it, where velocities decreased to below  $0.25 \text{ m s}^{-1}$ . The mean  $\bar{u}^*$  around the eddy is  $6 \text{ cm s}^{-1}$ , which can be considered the mean translation speed of the eddy. By contrast the average speed of the float circumnavigating the eddy is  $0.22 \text{ m s}^{-1}$ . The float rose by 60 dbar when caught in the eddy. After leaving the eddy it was again caught up a high velocity current, translating at  $0.9 \text{ m s}^{-1}$  with  $\bar{u}^*$  of  $0.55 \text{ m s}^{-1}$ . After two days in the current it spun off to the north side of the current and was caught in a recirculation until the end of its mission. The recirculation speeds were  $0.25 - 0.5 \text{ m s}^{-1}$  for  $u_{\text{RAFOS}}$  and  $0.25 \text{ m s}^{-1}$  for  $\bar{u}^*$ .

The temperature was warmest ( $7.5-9^\circ\text{C}$ ) right after deployment and when float 7 was in the regions of strong velocity. When it was at the northern side of the first eddy and once it started recirculating at  $43.5^\circ\text{N}$   $42^\circ\text{W}$  the temperature lowered to  $6-7^\circ\text{C}$ . The total number of half turns are consistently 25–50 per 4 hour period, except for a brief period before right after launch. The ddt values are below 0.5 for all of the mission but for two spikes. As the float moved from the eastward branch to the recirculation at  $43.5^\circ\text{N}$   $42^\circ\text{W}$  the surrounding water moved upward roughly 100 m. The values of  $|u_{\text{EF}}|/|\bar{u}^*|$  for this float are close to 1, even when the float is in the strong velocity maxima of the current, though the values range from close to 0 to 2.

The trajectory of float 10 was similar to that of float 7, but more data gaps prevent a detailed evaluation. At its equilibrium depth of 900 m the velocity was more barotropic than baroclinic. It was quickly entrained in a high velocity current after deployment, though it only shows speeds of  $0.61$  and  $0.41 \text{ m s}^{-1}$  for  $u_{\text{RAFOS}}$  and  $\bar{u}^*$ . Though a ten day gap follows, the shape of the track and the similarity to float 7 suggest that this float also transited around the same eddy located at  $43.3^\circ\text{N}$  and  $43.9^\circ\text{W}$ , perhaps making multiple loops since float 7 completed its one loop in only 5 days. The float exited the eddy to

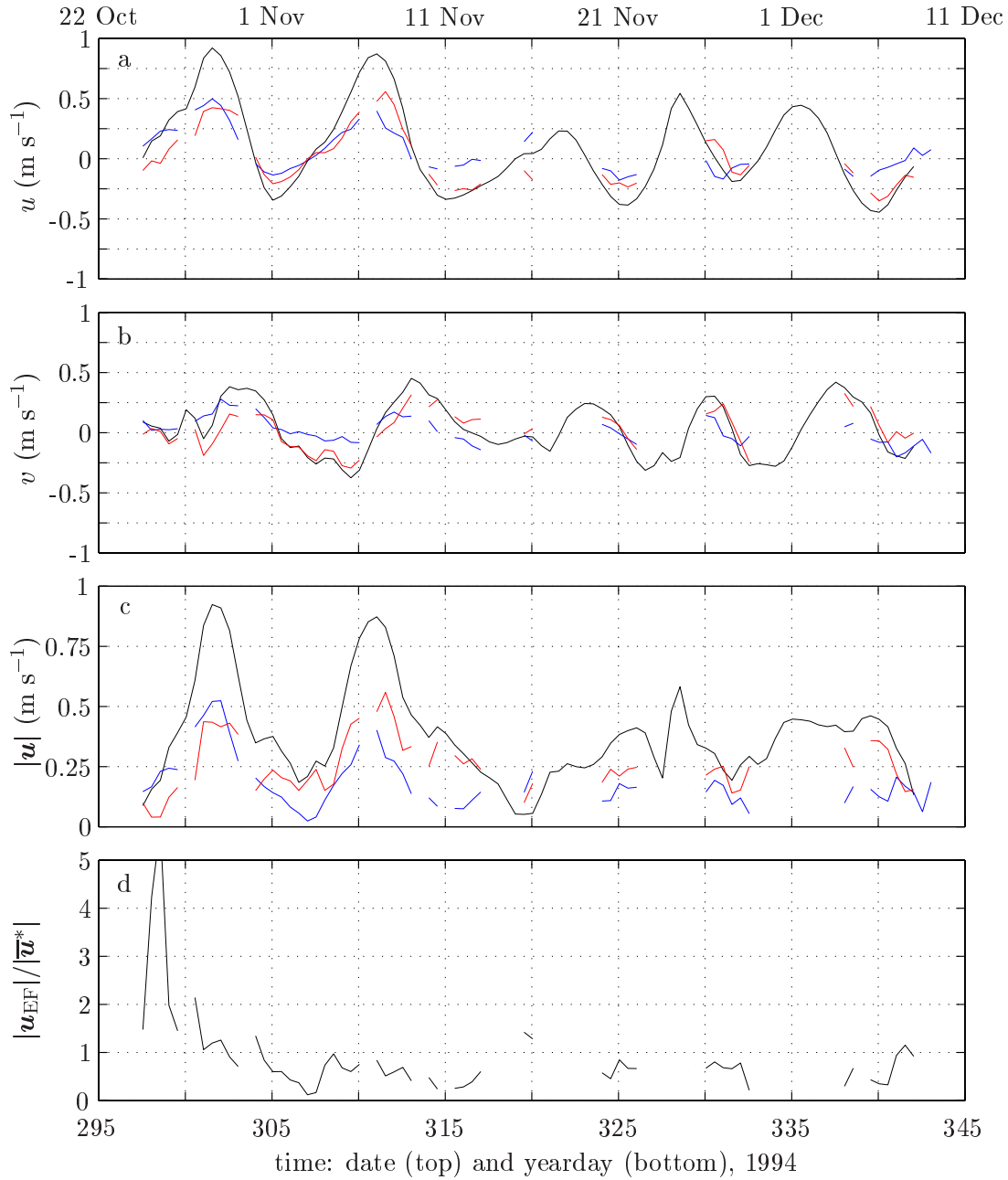


Figure 3.2: Time series of raw data for float 7: (a) and (b) show the  $u$  and  $v$  components of  $\mathbf{u}_{\text{RAFOS}}$  (black),  $\mathbf{u}_{\text{EF}}$  (blue), and  $\bar{\mathbf{u}}^*$  (red); (c) the speed of  $\mathbf{u}_{\text{RAFOS}}$ ,  $\mathbf{u}_{\text{EF}}$ , and  $\bar{\mathbf{u}}^*$  (same colors as above); (d)  $|\mathbf{u}_{\text{EF}}|/|\bar{\mathbf{u}}^*|$ , the ratio of baroclinic to barotropic velocity at the float's depth. The data in subplots a–d are sampled every 12 hours.

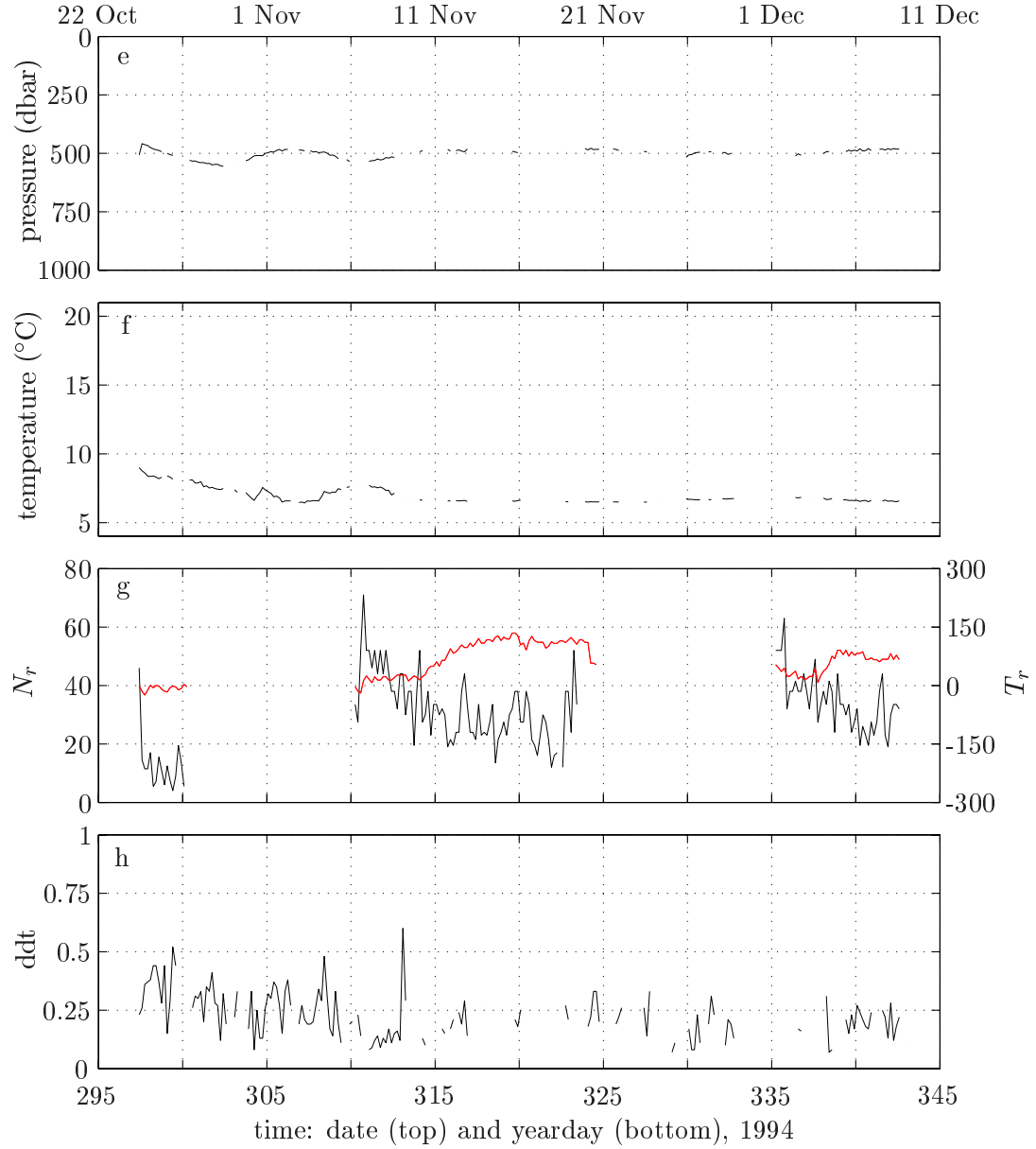


Figure 3.2: (continued) (e) pressure in; (f) temperature; (g) the total number of half-turns  $N_r$  (black) and the total summed half-turns  $T_r$  (red); and (h) ddt, a measure of the quality of the numerical fitting of  $\mathbf{u}_{\text{EF}}$ . The data in subplots e–f are sampled every 4 hours. See text for details of  $N_r$ ,  $T_r$ , and ddt.

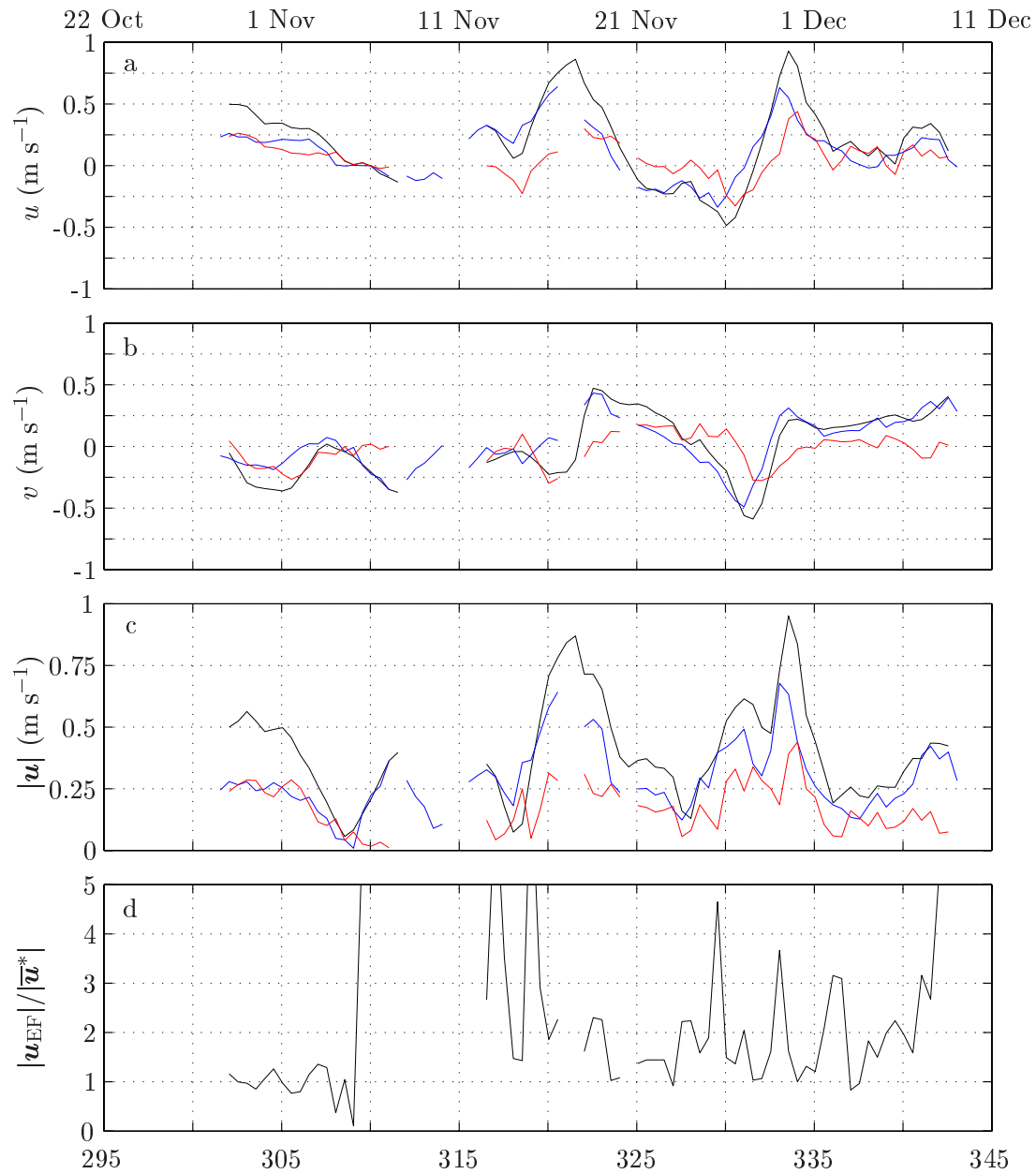


Figure 3.3: Time series of raw data for float 8. See Figure 3.2 for caption.

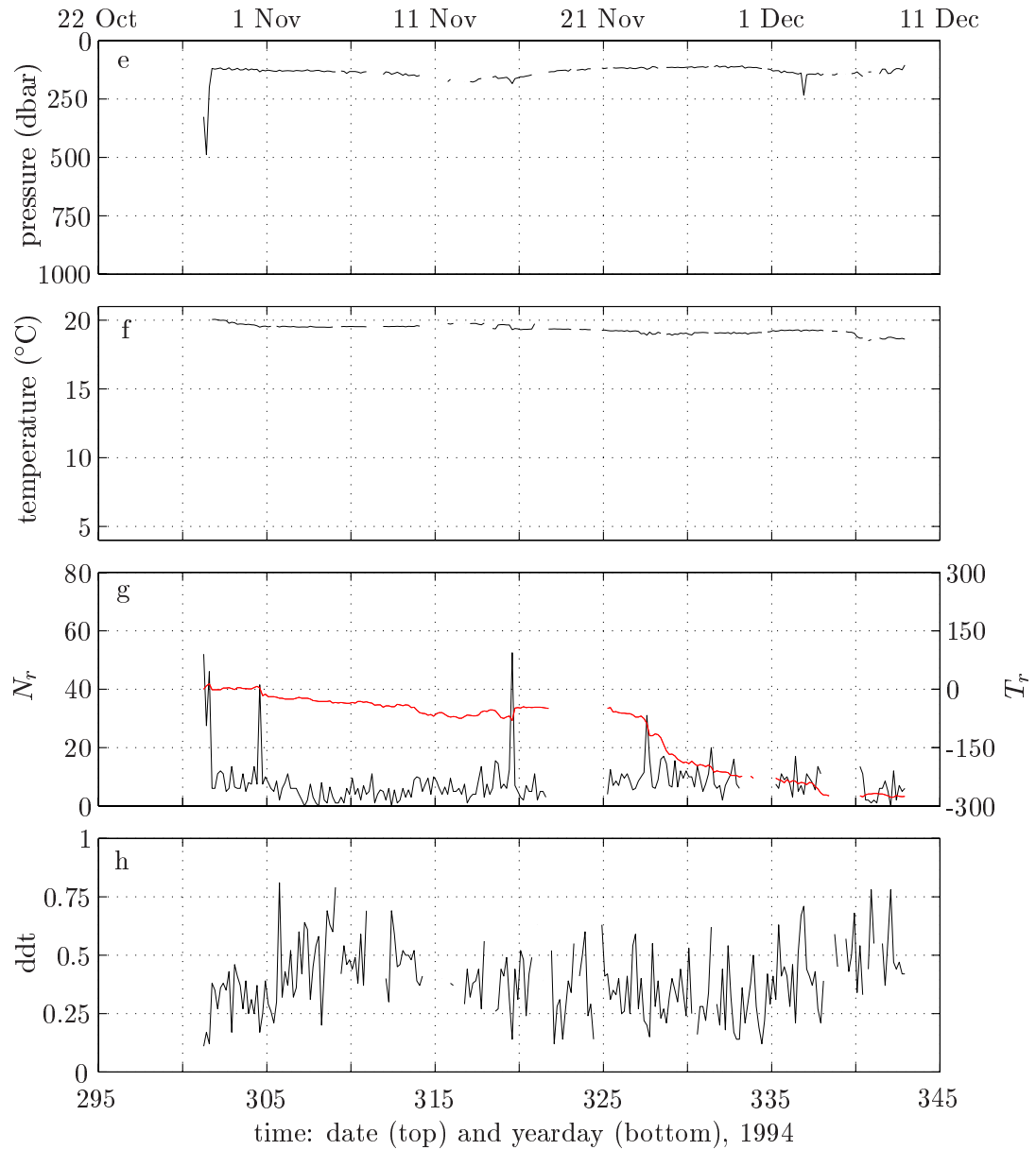


Figure 3.3: (continued)

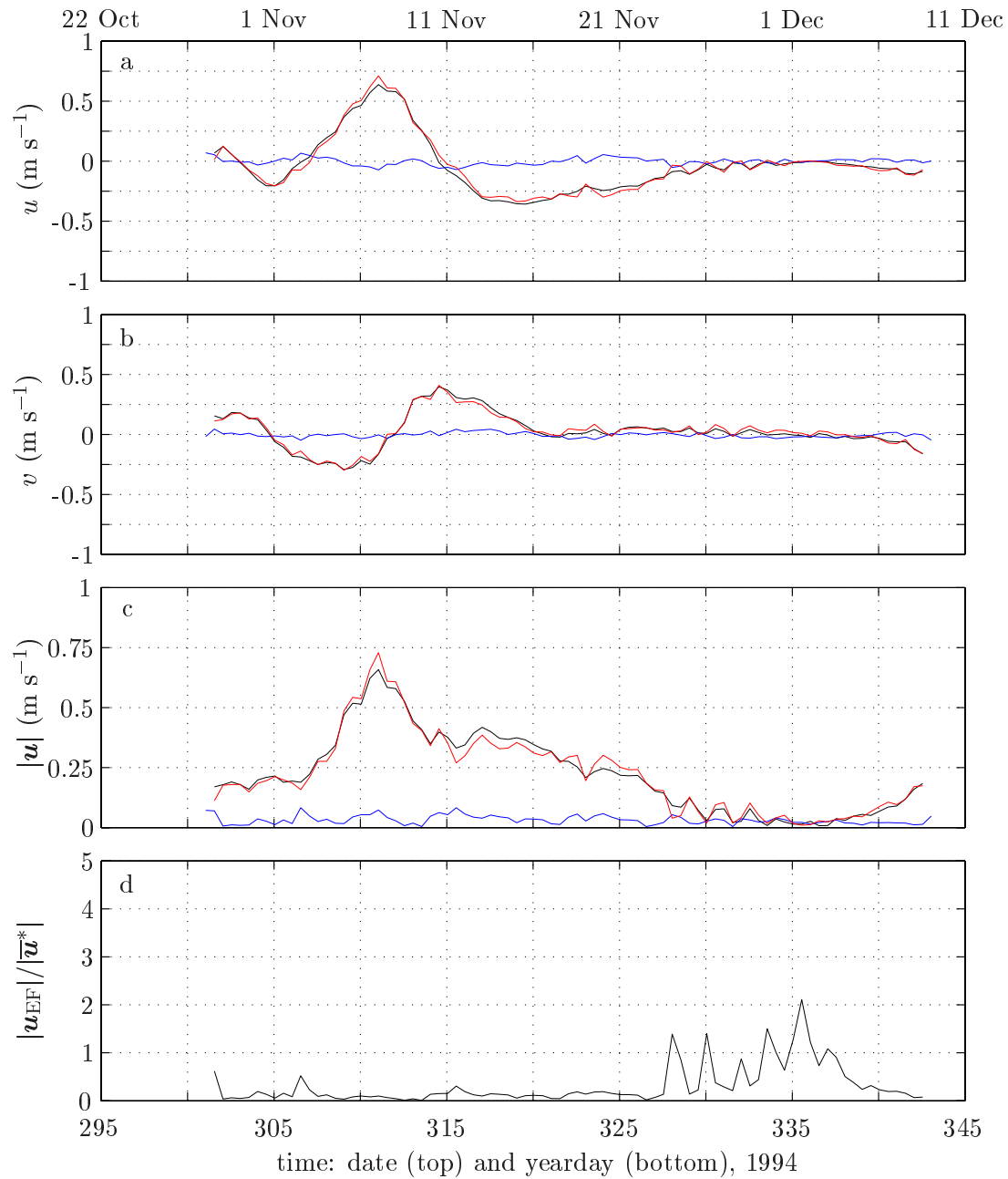


Figure 3.4: Time series of raw data for float 9. See Figure 3.2 for caption.

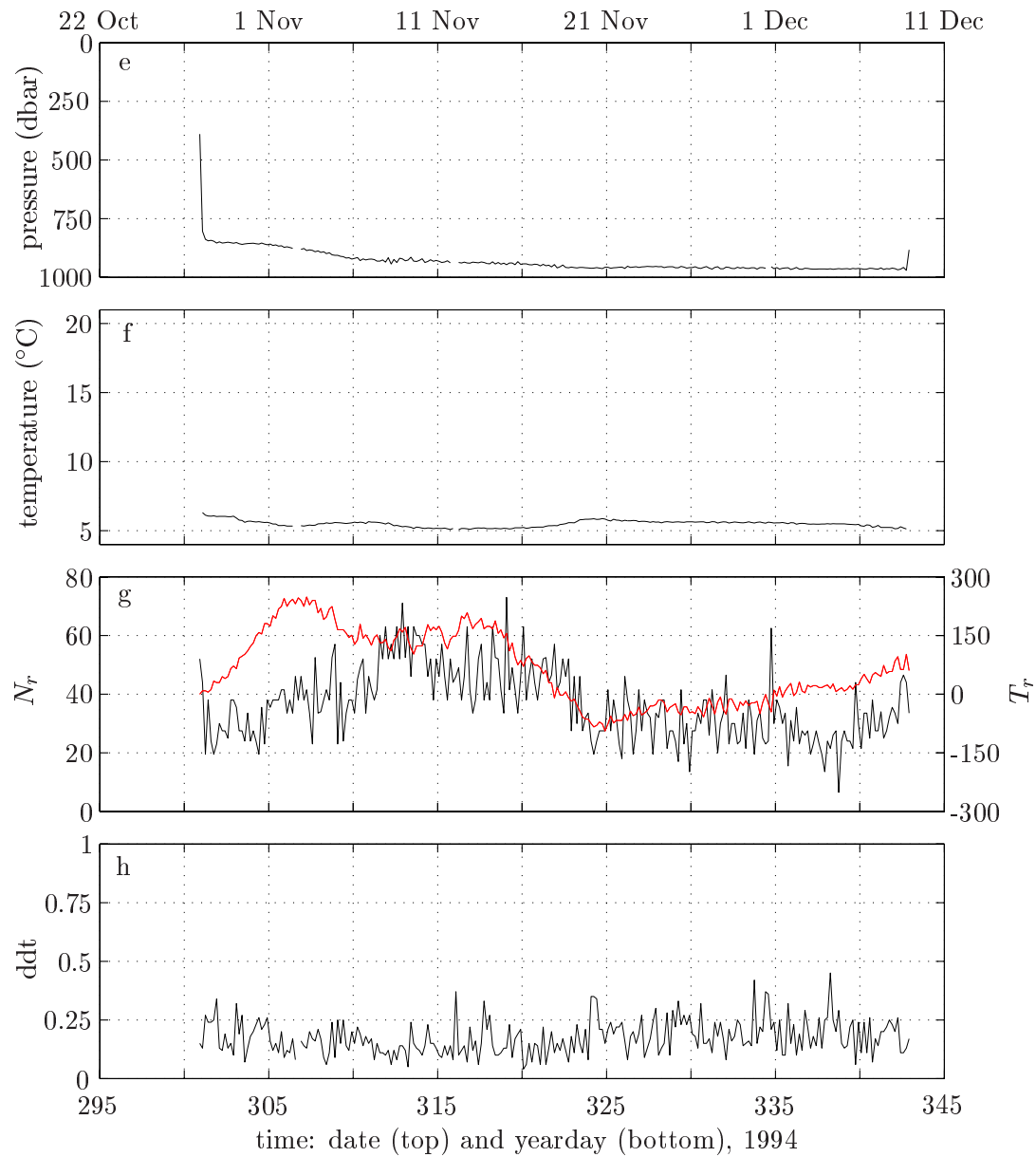


Figure 3.4: (continued)

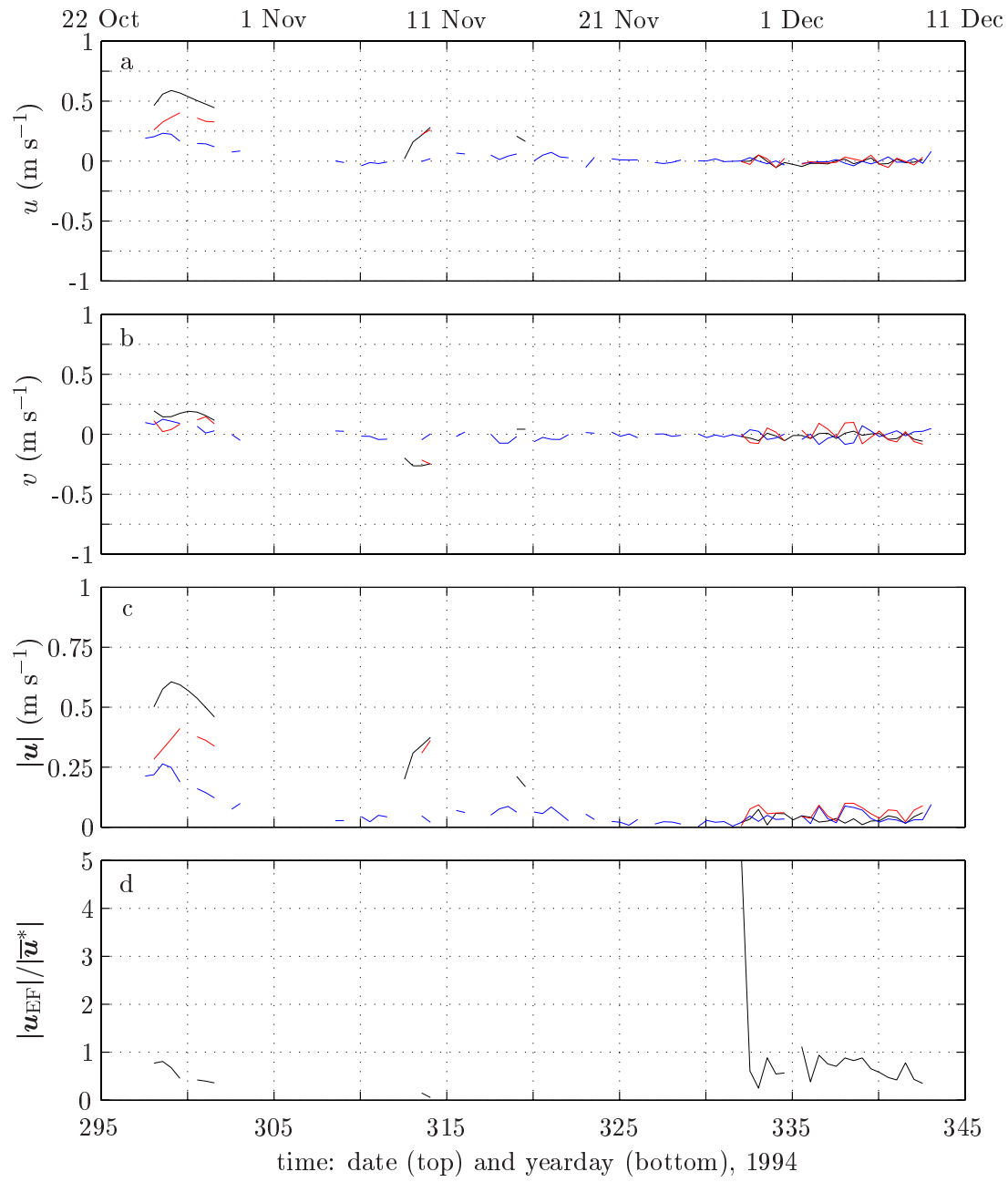


Figure 3.5: Time series of raw data for float 10. See Figure 3.2 for caption.

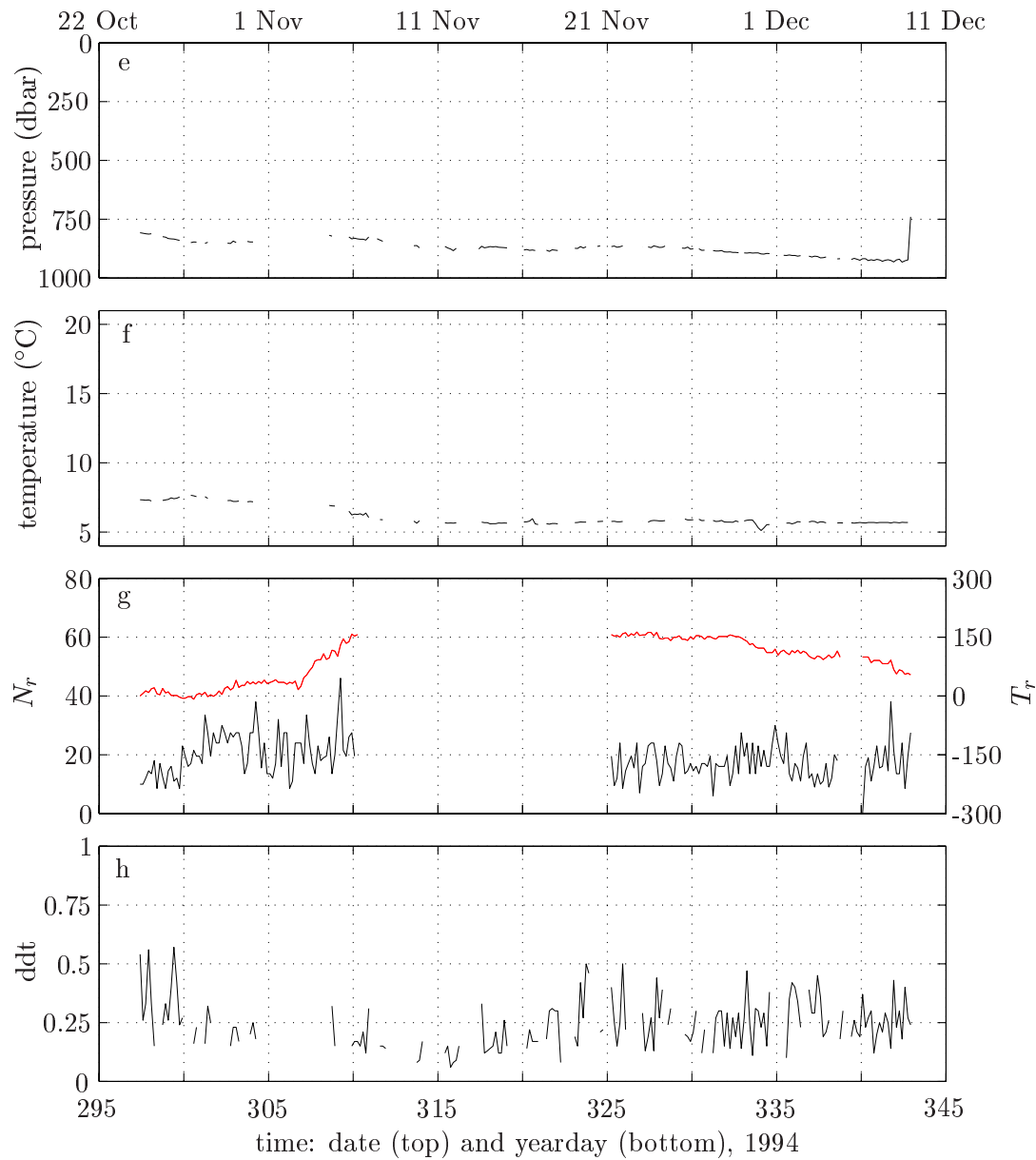


Figure 3.5: (continued)

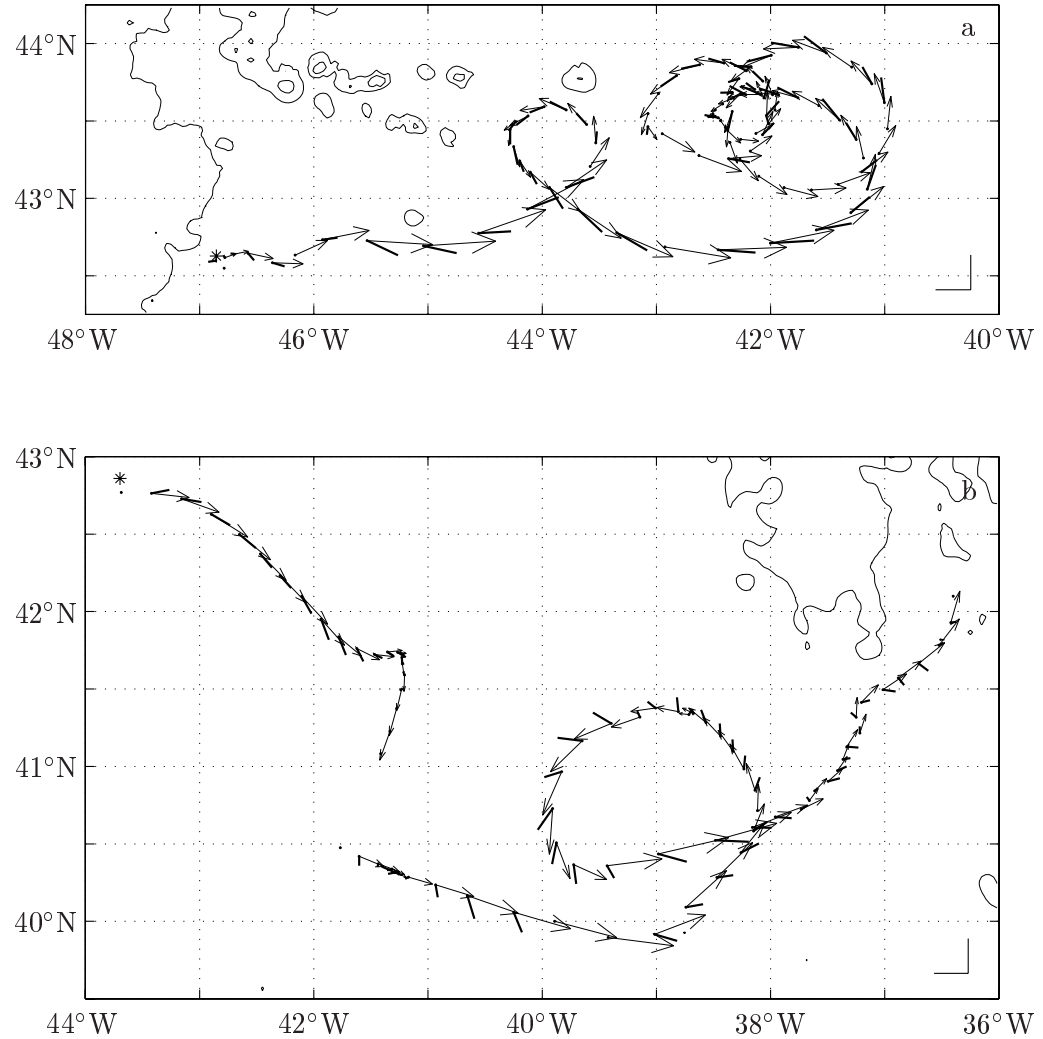


Figure 3.6: The trajectories and velocities at 12 hour intervals for all EFFs: (a) float 7, (b) float 8, (c) float 9, and (d) float 10. The launch positions are indicated by \*,  $\mathbf{u}_{\text{RAFOS}}$  by the thin arrows, and  $\bar{\mathbf{u}}^*$  by the thick lines. Velocity scales of  $0.5 \text{ m s}^{-1}$  are shown in all figures at the bottom right ( $u$  and  $v$  scales are the same), all plots are at the same geographic scale, and bottom contours are at 3000 and 4000 m (Smith and Sandwell, 1997).

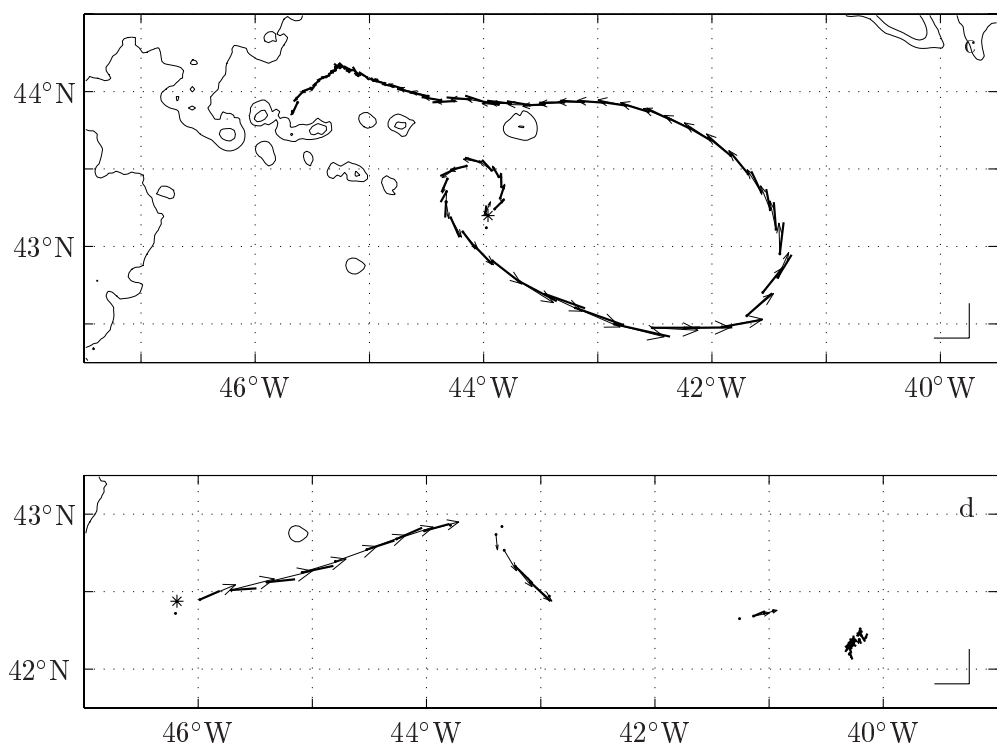


Figure 3.6: (continued)

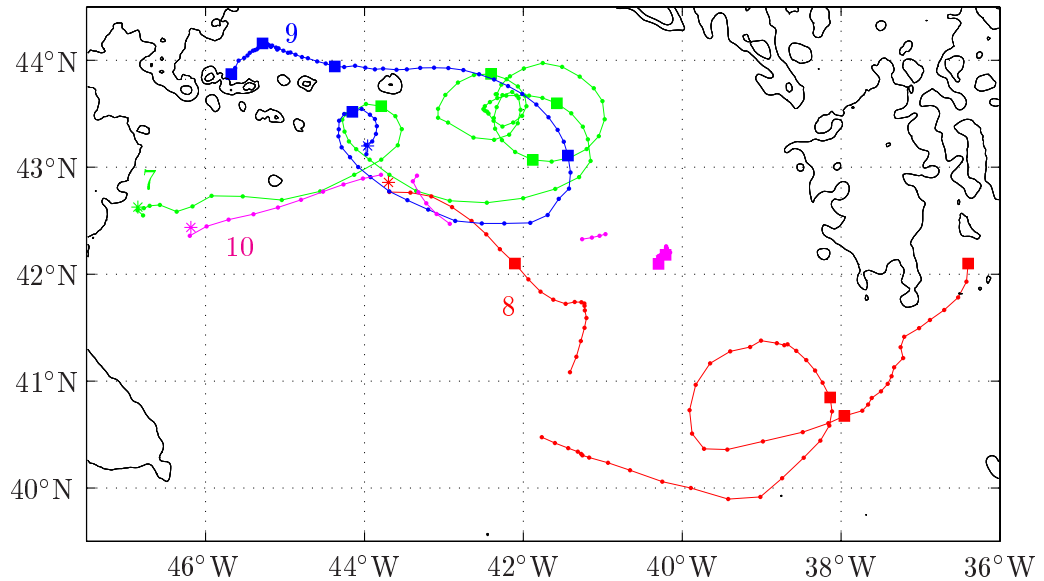


Figure 3.7: The trajectories of all EFFs (labeled). The launch positions are indicated by \*, 12-hour position fixes are shown by ·, larger markers ■ occur every 10th day (on Nov 1, 11, 21, and Dec 1), and the bottom contours are at 3000 and 4000 m (Smith and Sandwell, 1997).

the south and turned to the east, appearing to leave the strong current after 6 days. At the end of its mission velocities are less than  $0.1 \text{ m s}^{-1}$  for  $\mathbf{u}_{\text{RAFOS}}$  and  $\bar{\mathbf{u}}^*$ , and there is almost no horizontal translation. Clearly the float left the main current, though it did so by going south with no apparent coherent structure.

Float 10 had total half turns of around 20 for most of its mission, with values of 10 for the first three days after launch. Similar to float 7, as it went from the strong jet to the presumed eddy at  $43.5^\circ\text{N}$   $44^\circ\text{W}$  north of the NAC water rose 100 m past the float. The ddt values are all below 0.5, but are slightly higher when the half-turns are small. The initial temperature after launch is  $7.5^\circ\text{C}$ . During the last 10 days when the float is stationary it is around  $5.5^\circ\text{C}$ . The values of  $|\mathbf{u}_{\text{EF}}|/|\bar{\mathbf{u}}^*|$  are below 1.

Floats 8 and 9 were released SE of the Labrador Seamounts, and, like floats 7 and 10, one (9) was released close to the center of the current while the second (8) was released 44 km south. Again, float 9 followed the current for longer before drifting shoreward of the current, and float 8 was detrained seaward early in its mission.

The circular loop made by float 9 immediately after launch shows that it started south of the same eddy with which floats 7 and 10 interacted. At its depth of 850–950 dbar the  $\mathbf{u}_{\text{RAFOS}}$  velocities were very close to barotropic for its entire mission, as shown by  $\mathbf{u}_{\text{EF}}$  being  $<8 \text{ cm s}^{-1}$  and averaging to  $3 \text{ cm s}^{-1}$ . Also, because it is moving at very close to the barotropic velocity,  $|\mathbf{u}_{\text{EF}}|/|\bar{\mathbf{u}}^*|$  values are very small during the first part of its mission (0.1–0.2). Only when the barotropic velocities became small did the baroclinic/barotropic ratio become  $\geq 1$ . Its average speed around the eddy ( $0.17 \text{ m s}^{-1}$ ) was similar to that of float 7. After escaping the eddy it was also entrained in a strong current that reached  $\mathbf{u}_{\text{RAFOS}}$  or  $\bar{\mathbf{u}}^*$  speeds of  $0.7 \text{ m s}^{-1}$ . Following the current as it turned north and then west, the velocities decreased to  $0.25 \text{ m s}^{-1}$ . Perhaps because of its greater depth it was not caught in recirculations like float 7. When it neared  $45^\circ\text{W}$  the velocities fell below  $0.1 \text{ m s}^{-1}$  and it drifted away from the current and approached the seamounts from the north. The last few measurements showed it accelerating toward the seamounts with  $\mathbf{u}_{\text{RAFOS}}$  and  $\bar{\mathbf{u}}^*$  reaching  $0.18 \text{ m s}^{-1}$  at the last measurement point.

Float 9 had very low ddt levels (around 0.2) during its entire mission. The total half-

turns were consistently large, from 25–50 per 4 hour period. The temperature was initially warm ( $6^{\circ}\text{C}$ ) when it started around the eddy. It too shows upward water motion when going to the inshore side of the first eddy, with a corresponding decrease on the opposite side. Between  $43^{\circ}\text{N}$  and  $44^{\circ}\text{N}$  there is large downward motion of the water. This motion is consistent with cyclonic motion on the onshore side of this meander. The temperature dipped a little before reaching of a low of  $5^{\circ}\text{C}$  as it did a  $180^{\circ}$  turn at  $41.5^{\circ}\text{W}$ . Upon becoming separated from the strong current the water warmed up to near  $6^{\circ}\text{C}$ .

The last float (8) was the shallowest, floating at depths of 100–175 dbar. Deeper depths at the first two 4 hour averages indicate that the corrodible link was still attached then. The initial  $\bar{u}^*$  measurement was close to  $0.3 \text{ m s}^{-1}$ , a speed which is much smaller than the maxima encountered by other floats. Despite the direction of the barotropic flow being to the ENE at first, the near surface currents carried the float to the southeast. This float trajectory is characterized by quicker changes in flow speed and direction than the deeper floats. It translated 500 km in an unsteady SE direction. The velocity of the float reached  $0.87 \text{ m s}^{-1}$ , but  $\bar{u}^*$  remained at or below  $0.25 \text{ m s}^{-1}$ . An eddy made it loop before heading off at smaller velocities toward the NE. The average barotropic velocity around the eddy was  $2 \text{ cm s}^{-1}$ , and the maximum barotropic velocity the float observed was  $0.44 \text{ m s}^{-1}$ . The eddy exhibits large downward water motion and is discussed further in section 5.1. This trajectory had baroclinic velocities consistently larger than the barotropic velocities, with the ratio being 1–7. The initial temperature of float 8 was near  $20^{\circ}\text{C}$ . As the float moved southeastward the temperature dropped gradually to  $19^{\circ}\text{C}$ .

The half turn data show a very small number of turns compared with other floats, which is expected due to the higher stratification at the surface and the resultantly smaller amplitude internal waves. Aside from large spikes at launch and at large pressure perturbations, the total half turns is 5–10 for 4 hour totals. This lack of rotation, particularly at yearday 310, could be responsible for the high ddt values.

### 3.4 Concurrent Data Sets

When the EFF floats were active there were many ongoing studies of the NAC. Data sets that are used in later analyses are introduced here: a hydrographic survey, a large deployment of isopycnal RAFOS floats, and inverted echo sounder data.

Hydrographic data were collected during and after EFF deployment (Clarke, 1994). The locations are plotted in figure 3.8 by circles. The analysis of section 4.4 uses the profiles that are represented by filled circles and the EFF data that are represented by dots.

Isopycnal RAFOS floats were co-deployed with certain EFFs and fully covered the NAC region as part of a study by Tom Rossby at the University of Rhode Island (URI) (Anderson-Fontana et al., 1996) — these floats shall be referred to as URI RAFOS floats. Qualitative comparisons can be made between EFF trajectories and URI RAFOS trajectories (section 4.2). The most applicable analysis to come out of this data set for the present study is a treatment of the statistical properties of the floats in Zhang et al. (2001).

Pressure-equipped inverted echo sounders (PIES) were stationed along a transect where EFFs 7 and 10 were deployed (Figure 3.8, and also Meinen and Watts, 1998, 2000). They operate by measuring round-trip travel time from the bottom to the top of the water column. Average specific volume anomaly ( $\delta$ ) profiles are uniquely determined by the acoustic travel time in an empirical fashion (called gravest empirical mode, GEM) that accounts for 95% of the variance between 200 and 1500 dbar (Meinen, 2001). Integrating  $\delta$  vertically to obtain geopotential height anomalies and differencing between stations gives the geostrophic relative velocity between stations. A bottom reference velocity is calculated by optimal interpolation of bottom pressure sensors and deep current meter data (Meinen and Watts, 2000). Combining the PIES/GEM geostrophic velocity with the absolute bottom velocity results in transects of absolute velocity profiles. Velocities when the floats were nearby were kindly provided by Meinen and Watts (2000). These data were filtered with a 40-hour low-pass filter and subsampled once per day.

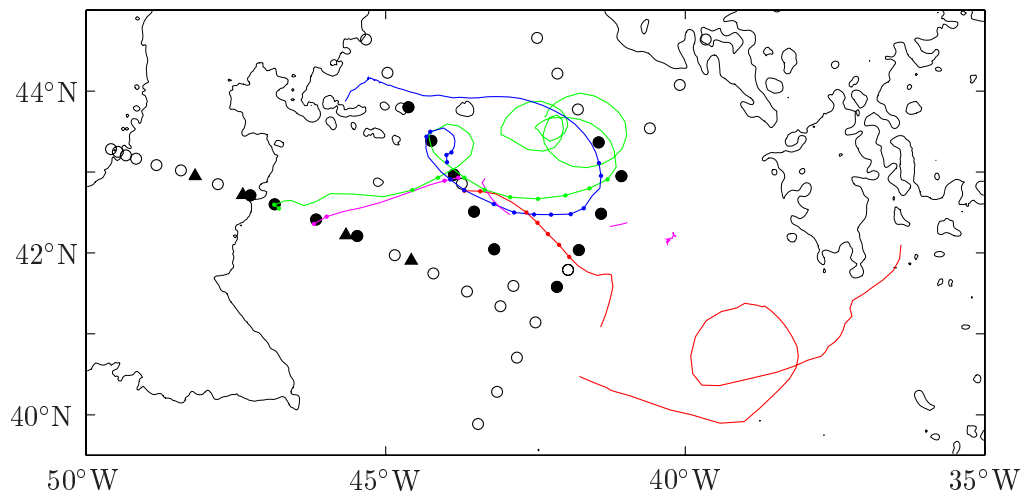


Figure 3.8: Additional data sets. CTD stations are shown as  $\circ$ , and those stations used in subsequent analysis shown as  $\bullet$  (see section 4.4). PIES sensors are shown by  $\blacktriangle$ . EFF trajectories are shown in the same colors as in Figure 3.7. Data points that are used in section 4.4 are shown by small dots. The 500 and 4000 m isobaths are shown (Smith and Sandwell, 1997).

## Chapter 4

### VALIDATION OF DATA

This chapter discusses the quality of the data from the EFF floats: the errors of system components, the observed path of URI RAFOS floats deployed concurrently with EFF floats, the error of  $\bar{u}^*$  between EFF floats, and comparisons with velocities calculated from hydrographic and inverted echo sounder data.

#### 4.1 *Error Analysis*

As EFFs contain two systems that obtain data separately, errors will arise independently in each of them. The two data streams are combined in the processing stage, from which we can propagate the raw errors to determine the instrumental precision of  $\bar{u}^*$ .

##### 4.1.1 *RAFOS System*

Errors introduced by the RAFOS system will affect the location fixes and hence the float velocities. Care has been taken to make the tracking consistent to avoid spikes in the velocity results by avoiding changing from one triplet of sound sources to another. Changing the sound sources used for calculating position changes the biases present and can result in discontinuous shifts of position.

The most significant source of error are clock drifts, for they will add a bias to all range calculations. Corrections for this must be applied to both the float clocks and the sound source clocks. After correction for clock drifts, moored RAFOS floats have been observed to have rms time offsets of 0.2–0.3 seconds for a given sound source (König et al., 1991). This fluctuation is most likely caused by changing oceanographic conditions between the source and the receiver. The above study was conducted in the Iberian Basin, where eddies of Mediterranean origin are frequently observed.

Errors in timing translate into errors in the range from the float to the sound source, but to get the two dimensional error the use of multiple sound sources must be considered. Three sound sources are necessary for 2-D tracking and hyperbolic correction of the float clock. Though below I consider the errors from two sound sources, using a third would eliminate errors associated with the float clock.

Horizontal errors will geometrically be largest when the angle between the two sound sources is small. For all the positions that the EFFs occupied, the worst angle that any EFF made with two sound sources is about  $25^\circ$ . The other 2 angles (only three sound sources gave usable signals) may be more acute than this. As each range yields a distance plus or minus an uncertainty, two concentric circles bound the region where the float is assumed to lie. With two independent range measurements, the intersection of the two pairs of circles forms a roughly parallelogram-shaped area that bounds the location of the float, dependent of course on the angle from the float to each sound source. The major and minor axes of this region are  $\pm 2.8$  and  $\pm 0.5$  km and are assumed to be independent of each other.

We are more concerned about the error in the RAFOS-derived velocity  $\mathbf{u}_{\text{RAFOS}}$ , however, which are centered differences over 24 hours. As shown later (section 5.3.1) the integral time-scale of  $\mathbf{u}_{\text{RAFOS}}$  is 1.5–2 days, so position fixes made 24 hours apart will tend to have the same oceanographic-derived biases. Thus, when differencing the positions, errors due to oceanographic conditions will partially cancel.

Accounting for these considerations gives an error in velocity of  $2 \text{ cm s}^{-1}$ . The error is the same as for commercial RAFOS floats. For floats deployed off of South Africa, Boebel and Barron (2003) cited errors in position of 10 km absolute and 2 km between relative positions, with a corresponding velocity error of  $2 \text{ cm s}^{-1}$ ; and for floats deployed in the North Atlantic during 1982–2001, Carr and Rossby (2001) mention an absolute position uncertainty of  $< 1$  km and a velocity uncertainty of  $\pm 1\text{--}2 \text{ cm s}^{-1}$ .

#### 4.1.2 EF System

Errors in the electric field system can come from electrode offsets, gain, electrode noise, amplifier noise, compass misalignments, or data that can only poorly be fit due to insufficient rotation.

Drifts of electrode offsets that are 2nd order polynomials in time are removed from the electric field measurements every four hour averaging period (see section 3.2). Raw data that cannot be accurately processed due to insufficient rotation are removed during the processing stages. The electrode resolution is equivalent to a velocity resolution of 3  $\text{mm s}^{-1}$ .

##### *Gain*

Care was taken in building the EFFs to reduce the electrode and amplifier noise. Aging the electrodes in a pressurized tank reduces their spectral noise level by about 15 dB. At rotation periods of less than one hour the amplifier is the largest source of noise compared to the aged electrodes. Jane Verrall carried out tests to determine the amplifier noise at different rotation rates. When averaging the measured potential over 8 hours, and when the float's rotation rate is once every 2, 10, and 60 minutes, the rms velocity is  $\leq 1 \text{ mm s}^{-1}$ . When the averaging interval is 2 hours, the rms velocity is 2  $\text{mm s}^{-1}$ . Thus, for an averaging period of 4 hours as was used in the NAC deployment, the expected  $\mathbf{u}_{\text{EF}}$  error is  $< 2 \text{ mm s}^{-1}$ . This error is on the same order as that introduced by digitizing the analog signal.

##### *Compass*

The compass deviations of the floats were measured at the NOAA Sand Point, Seattle compass range, and were included in the program the floats ran while deployed. Ideally the compass alignment could be heuristically tested from the data, but because of the small set of observations there is not enough statistical certainty to do so. Full transits around an eddy were made twice by floats 7 and 8. Averaging  $\bar{\mathbf{u}}^*$  around the eddy gave the barotropic translation velocity of the eddy: in both cases this was smaller than the

speeds observed as the float went around the eddy and were consistent with the observed evolution of the eddies. The eddy was relatively close to non-divergent, aside from the reasonable translation, so compass offsets would not heuristically improve the expectation of non-divergence.

#### 4.1.3 *Combined Error*

The errors in the EF and the RAFOS system are independent, arising from different sources so they can be assumed independent and added in quadrature for estimating the uncertainty of  $\bar{u}^*$ . The RAFOS error will dominate because it is an order of magnitude larger than the EF errors, yielding an expected error of  $2 \text{ cm s}^{-1}$ .

### 4.2 *Comparison to URI floats*

Isopycnal RAFOS floats were deployed at the same locations as EFFs 7 and 10 by investigators at the University of Rhode Island (URI). Four were deployed with EFF 7 (Figure 4.1), two each at potential densities of 27.2 and 27.5  $\sigma_\theta$  (URI RAFOS floats 324 and 328 at 27.2  $\sigma_\theta$ , and 333 and 339 at 27.5  $\sigma_\theta$ ; see Anderson-Fontana et al., 1996). The shallower floats have similar trajectories until reaching the eddy at  $46^\circ\text{W}$ . They rose 100–150 dbar from 500 dbar while they did a half revolution around the eddy and headed west out of it, never making a full revolution. The deeper floats show no influence of the eddy — they headed east in a strong current past  $42^\circ\text{W}$ , after which other flow features interacted with them. They were at depths of 700–800 dbar. URI RAFOS 339 made one revolution in the recirculation where float 7 spent the end of its mission, after which its track followed that of EFF 9 before heading further to the north; and URI RAFOS 333 detrained from the NAC close to where EFF 8 did so. EFF 10 and URI RAFOS 332 (at 27.5  $\sigma_\theta$ ) remained close to each other for the first 5 days after launch (Figure 4.2). Despite an apparent divergence in paths, which is obscured by data gaps in EFF 10's trajectory, both floats were ultimately caught in the same region of weak flow at  $42.5^\circ\text{N}$   $40.5^\circ\text{W}$ .

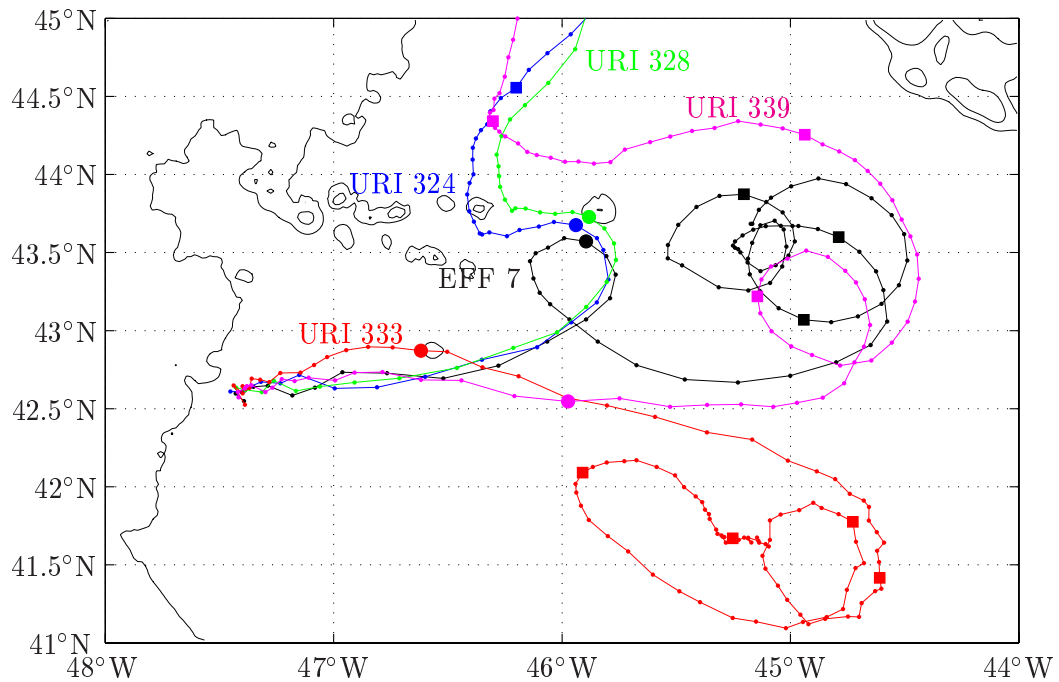


Figure 4.1: EFF 7 (black) and URI RAFOS floats (colored) launched at the same time. The position at yearday 305 (1 Nov) is shown by a large  $\bullet$ , and each 10 day increment thereafter by  $\blacksquare$ . URI RAFOS floats 324 and 328 are at  $\sigma_\theta = 27.2$ , and 333 and 339 are at  $\sigma_\theta = 27.5$ . For clarity, URI RAFOS trajectories are only shown up to yearday 350 (16 Dec).

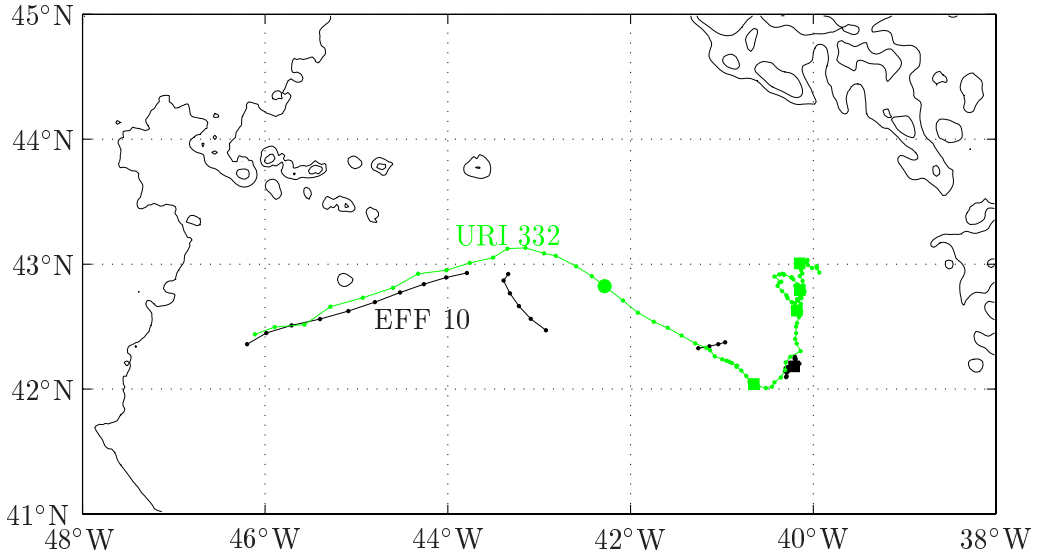


Figure 4.2: EFF 10 (black) and a URI RAFOS float (green) launched at the same time. URI RAFOS float 332 was deployed at  $\sigma_\theta = 27.5$ . Otherwise the same as Figure 4.1.

### 4.3 EFF Intercomparisons

The precision of  $\bar{u}^*$  can be seen by comparing measurements taken when two floats are close in space and time. If two floats are at the same location at the same time the only errors will be due to instrumental sources. As the measurements become further separated with distance and time, oceanic variability will be increasingly important and  $\bar{u}^*$  from different floats will naturally differ more and more. The oceanic variability is defined by autocorrelation sequences of the velocity field, for which the statistical properties need to be determined by either heuristically from data or by making simplifying assumptions.

Zhang et al. (2001) showed that removal of the time mean velocity field in the NAC region produces eddy velocities that fit Gaussian statistics. The absolute velocities on isopycnal surfaces that they calculate, however, are neither directly transferable to isobaric EFFs nor to measurements of  $\bar{u}^*$ . They do find that the eddy fields are coherent with depth (from  $\sigma_\theta$  of 27.2 to 27.5), so we expect  $\bar{u}^*$  to have statistical processes similar to

their findings. Other studies of Lagrangian floats (Bracco et al., 2000) found that without removing the mean velocity field the distribution of speeds fit an exponential distribution instead.

With only four floats the robustness of statistical calculations needs verification. Though there is not enough spatial or temporal coverage to calculate mean velocity fields with EFF data, the Lagrangian time series are well representative of the flow (see section 5.3.1), and exhibit behavior expected from turbulence theory.

The distribution of  $\bar{u}^*$  for all measurements is not isotropic: there are more and larger  $\bar{u}^*$  in the positive direction than in the negative direction, but  $\bar{v}^*$  is evenly distributed. All of the floats were deployed in a fast eastward current, so this is expected. The distributions suggest high peaks (at  $\bar{u}^*, \bar{v}^* = 0$ ) and high tails, e.g. an exponential distribution, but the distribution is not well-determined enough to distinguish between exponential or Gaussian distributions (data not shown).

The first way to see how well the  $\bar{u}^*$  measurements compare between floats was to compare  $\Delta\bar{u}^*$  and  $\Delta\bar{v}^*$  against the time ( $\Delta t$ ) and space ( $\Delta r = [(\Delta x)^2 + (\Delta y)^2]^{1/2}$ ) differences between the measurements. There were too few measurement pairs to give an even spread of  $\Delta t$  values for  $\Delta r = 0$  km, or for an even spread of  $\Delta r$  values for  $\Delta t = 0$  days, so non-zero limits had to be adopted. When using  $\Delta r$  as the independent variable  $\Delta t$  was limited to  $\leq 1$  day, and when using  $\Delta t$  the limit was  $\Delta r \leq 15$  km. Both limits are less than the integral time- and length-scales calculated in section 5.3.1. The root mean square (rms) difference was calculated for each component of velocity and the results were binned according to the independent variable. The average and standard error of the mean for each bin are shown in Figure 4.3a,b, and the number of data points in each bin is in Figure 4.3c,d.

Organized turbulent flow exhibits 2 regimes: the first is when turbulent scales are dominant and turbulent properties increase rapidly (small  $t$ ), and the second is when the average organized flow dominates (large  $t$ ). The latter regime is of greater concern here, as the former is not well resolved by 12 hour measurements nor by floats deployed separately.

The small time-scale regime applies before the energy-containing scale is reached, when

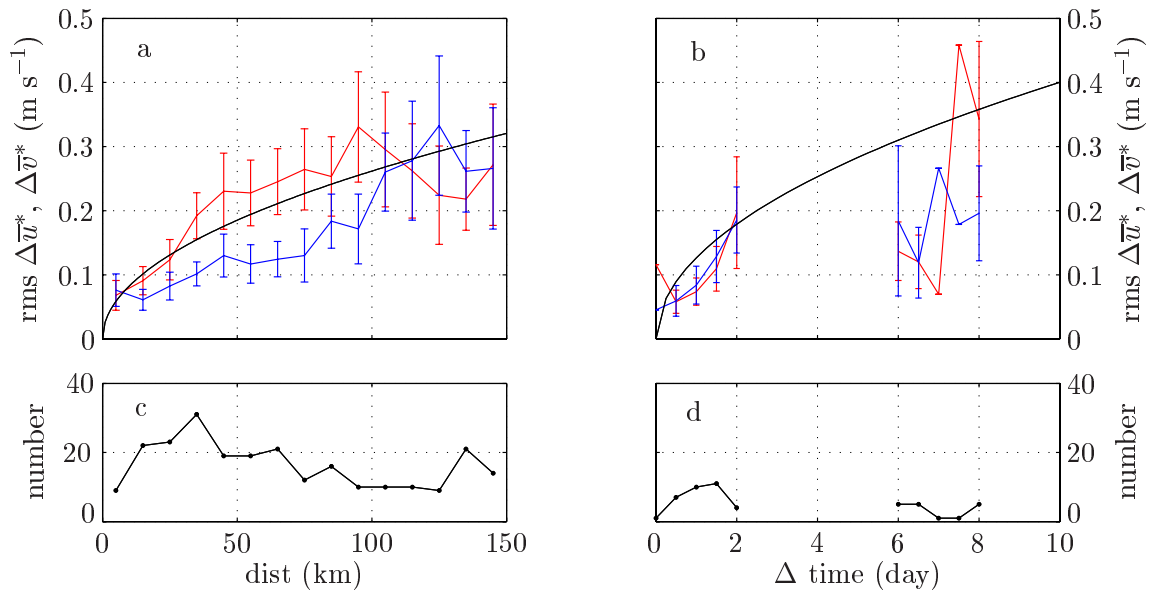


Figure 4.3: The rms  $\Delta \bar{u}^*$  versus distance (a) and time (b) between measurements, with the standard error of the mean ( $\sigma_{\Delta \bar{u}^*}$ ) being shown by the error bars. The  $\bar{u}^*$  component is red, and  $\bar{v}^*$  is blue. The data are binned every 10 km or 1 day, and rms  $\Delta \bar{u}^*$  and  $\sigma_{\Delta \bar{u}^*}$  are calculated in each bin. The number of data points per bin are shown in (c) and (d). With distance as the independent variable, the pairs are no more than 15 km apart, while with time, the pairs are no more than 1 day apart. The black lines show a  $\Delta t^{1/2}$  and  $\Delta r^{1/2}$  dependence for reference, which is expected for geostrophic turbulence. See text for details.

the particle-pair still retains memory of its initial displacement. For locally homogeneous 2-D turbulence the relative velocity should grow quadratically with time (LaCasce and Bower, 2000), or if the flow is also a turbulent enstrophy cascade then there will be an exponential time dependence of relative velocity. LaCasce and Bower (2000) found initial growth regimes for times smaller than 2 days, and in practice the exponential regime is found at intermediate time scales.

At larger separations the organization of the flow takes over. Zhang et al. (2001) found a regime that is linear with time for square turbulent float velocities, corresponding to a random walk process. Likewise, LaCasce and Bower (2000) described the same regime as energy cascading to larger scales. This growth would continue until the energy-containing scale is reached, at which point the mean-square relative velocity becomes constant at  $4E$  or  $2\overline{u'^2}$  (Babiano et al., 1990; LaCasce and Bower, 2000; Er-El and Peskin, 1981). The float missions were not long enough to reach this asymptote. Similar dependencies for relative displacement can be motivated by treating relative displacement as proportional to time multiplied by  $\overline{u'^2}$ .

The region in which the EFFs drifted may be more effectively considered as a subset of regions others have used (Zhang et al., 2001; LaCasce and Bower, 2000). The main region of peak velocities observed by EFFs was an eastward flowing part of the NAC. Greater anisotropy between the zonal and meridional directions is expected since there is little spatial averaging. Here the mean velocity structure is largest in the zonal component, so the meridional component of velocity  $\overline{v}^*$  should be closer to isotropic due to smaller mean velocities and should follow the  $t$  dependence more closely than the  $\overline{u}^*$  component.

In Figures 4.3a,b we can see that the rms velocity difference is consistent with a  $t^{1/2}$  dependence for separations in time and space, implying a turbulent energy cascade. Though there may be a steeper dependence on time for small values, these scales are not well resolved. The error bounds decrease to  $\pm 0.03 \text{ m s}^{-1}$  at the origin, and generally as the floats approach each other the rms difference and its standard error decrease. Figures 4.3c,d show the number of pairs per bin. Though the small sample size is especially obvious for the differences versus time, the differences versus distance have  $\sim 10$  data points or

more in all bins. Using non-zero limits for the second independent variable (e.g.  $\leq 1$  day or  $\leq 10$  km) results in non-zero y-intercepts. For the distance comparison the y-intercept has a value of  $5-7\pm3$  cm s $^{-1}$ , which is consistent with that for the time comparison.

Figure 4.3a,  $\sigma_{\Delta\bar{u}^*}$  against  $\Delta r$ , shows that as the floats get closer to each other in space the standard error of the mean decreases. Using a non-zero limit in time between measurements makes the data have a non-zero variance at  $\Delta t = 0$  km, even if the instruments were exactly precise. It does tend to a small value, however, about 5 cm s $^{-1}$  peak-to-peak. The same variable but against  $\Delta t$  highlights the small data set: there are gaps in the measurements, and some bins have only one value, hence  $\sigma_{\Delta\bar{u}^*}$  is zero. The values close to the origin are also small, however, giving us confidence that different floats measure the same quantity.

At the origin it is possible to calculate the expected rms difference. I define the true velocity field as a mean velocity plus an eddy velocity

$$\bar{u}_T^*(\mathbf{x}, t) = \bar{u}_{T,f}^*(\mathbf{x}) + \bar{u}_{T,e}^*(\mathbf{x}, t) \quad (4.1)$$

where  $\bar{u}_{T,f}^*$  is the fixed velocity field (averaged over time at a fixed location) and  $\bar{u}_{T,e}^*$  is an eddy velocity field that has a zero mean and a standard deviation of  $\sigma_{\bar{u}_{T,e}^*}$ . The  $j$ th measurement by the  $i$ th EFF consists of the true velocity ( $\bar{u}_T^*$ ), the fixed instrument bias ( $\beta$ ), and a random error ( $\epsilon$ ) of zero mean and standard deviation  $\sigma_\epsilon$ :

$$\bar{u}_i^*(\mathbf{x}_j, t_j) = \bar{u}_T^*(\mathbf{x}_j, t_j) + \beta_i + \epsilon_i(t_j)$$

The mean-square velocity difference is then written as  $\overline{(\bar{u}_{i_1}^*(\mathbf{x}_{j_1}, t_{j_1}) - \bar{u}_{i_2}^*(\mathbf{x}_{j_2}, t_{j_2}))^2} = \overline{\Delta\bar{u}^*}^2$ . For large spatial separations it is necessary to know the mean  $\bar{u}^*$  velocity field because it is anisotropic. Since this is not possible with our data, we need to make the restriction that  $|\Delta\mathbf{x}|$  be close to 0 so that  $\Delta\bar{u}_{T,f}^* = 0$  and thus  $\Delta\bar{u}_T^* = \Delta\bar{u}_{T,e}^*$ . Then, letting  $t_{j_1} \rightarrow 0$  and  $t_{j_2} - t_{j_1} \rightarrow \tau$

$$\begin{aligned} \overline{\Delta\bar{u}_T^*}^2 &= \overline{\Delta\bar{u}_{T,e}^*}^2 \\ &= \overline{\bar{u}_{T,e}^*}^2(0) + \overline{\bar{u}_{T,e}^*}^2(\tau) - 2\bar{u}_{T,e}^*(0)\bar{u}_{T,e}^*(\tau) \\ &= 2\sigma_{\bar{u}_T^*}^2 \left[ 1 - r_{\bar{u}_T^*}(\tau) \right] \end{aligned}$$

where  $r_{\bar{u}_T^*}(\tau)$  is the autocorrelation sequence of  $\bar{u}_T^*$  with lag  $\tau$ . Also note that  $\Delta\epsilon^2 = \frac{\epsilon_1^2(0) + \epsilon_1^2(\tau) - 2\epsilon_1(0)\epsilon_1(\tau)}{\epsilon_1^2(0) + \epsilon_1^2(\tau)} = 2\sigma_\epsilon^2$  because the error between two floats is uncorrelated. The expected square value of the difference of two velocity measurements becomes

$$\overline{\Delta u^{*2}} = 2\sigma_{\bar{u}_T^*}^2 [1 - r_{\bar{u}_T^*}(\tau)] + \overline{\Delta\beta^2} + 2\sigma_\epsilon^2$$

As  $\overline{\Delta\beta^2}$  cannot be calculated without more direct measurements, I assume it to be zero and obtain a limit on  $\sigma_\epsilon^2$ :

$$\sigma_\epsilon^2 \leq \overline{\Delta u^{*2}} - 2\sigma_{\bar{u}_T^*}^2 [1 - r_{\bar{u}_T^*}(\tau)]$$

This can only be applied for  $\Delta x = 0$ , because we can estimate  $r_{\bar{u}_T^*}(\tau)$  from statistics but not  $r_{\bar{u}_T^*}(\Delta x)$ . In practice Figure 4.3a,b is composed of measurements taken up to 1 day apart, so the term due to  $\overline{\Delta u_T^{*2}}$  will be averaged for  $\tau = [0, \frac{1}{2}, 1]$ . I use the autocorrelation function calculated in section 5.3.1. The standard deviation of  $\overline{\bar{u}_T^{*2}}$  is hard to define since the mean velocity structure is unknown. From the  $\bar{u}^*$  data the variance is  $4.4 \times 10^{-2}$  and  $1.8 \times 10^{-2} \text{ m}^2 \text{ s}^{-2}$  for  $\bar{u}^*$  and  $\bar{v}^*$ , but because  $\bar{u}^*$  is expected to have a smaller velocity than  $\mathbf{u}_{\text{RAFOS}}$  the eddy velocity variance is expected to be less than the mean-removed result of  $2.3 \times 10^{-2} \text{ m}^2 \text{ s}^{-2}$  found by Zhang et al. (2001). To be conservative I shall use  $2 \times 10^{-2} \text{ m}^2 \text{ s}^{-1}$ . The values of  $(\overline{\Delta u_T^{*2}})^{1/2}$  for the above  $\tau$  and with the mean square velocities of Zhang et al. (2001) are 0, 8, and  $12 \text{ cm s}^{-1}$ . The values used in the binning are evenly spread between  $\Delta 4$  or 0,  $1/2$ , and 1 day, so the expected oceanic variability is the average of these values, or  $7 \text{ cm s}^{-1}$ . Because of uncertainty a range of  $6\text{--}10 \text{ cm s}^{-1}$  is reasonable.

At the origin of Figure 4.3c we can estimate the instrumental error. The y-intercept estimated graphically is around  $7 \text{ cm s}^{-1}$ . Using the above approximations the error in the floats' rms  $\bar{u}^*$  at the origin is of the same order as that expected from the turbulent flow. Though all of this error could be easily explained by oceanic variability, it also is the upper limit for  $\sigma_\epsilon$ . At most a fraction of the y-intercept is due to instrument error ( $0\text{--}5 \text{ cm s}^{-1}$ ). Dividing by  $\sqrt{2}$  gives the error of a single measurement as  $0\text{--}4 \text{ cm s}^{-1}$ .

#### 4.4 Comparisons to Absolute Geostrophic Velocities

The hydrographic data that was collected when the EFFs were deployed allows a comparison between the velocities measured by the floats and those calculated by the geostrophic method. The two techniques are comparable in that they are both integrative ways to calculate the velocity that involve horizontal spatial averaging. The CTD stations and the float data used in this analysis is graphed in Figure 3.8.

Any float trajectory that went between two profiles was used if the time difference was small for the flow regime at that point: e.g. if the flow was fast or changing quickly smaller time differences were accepted than for stable and slow currents. Multiple float measurements ( $u_{\text{RAFOS}}$  and  $\bar{u}^*$ ) were averaged to reduce time variability. Only the component of velocity resolvable by geostrophic calculations (notated as  $u$ ) could be compared; it was determined by vector rotations of the EFF velocities. Similarly, no restriction was taken on the angle of the float path relative to the CTD pair because  $\bar{u}^*$  data are two dimensional. The geostrophic velocity between two stations was calculated with the hydrographic data, as was the electrical conductivity-velocity covariance. The velocity of the float ( $u_{\text{RAFOS}}$ ) was used as a reference to make the geostrophic velocities absolute.

The CTD profiles in any pair are taken close to each other in time; six of them differ by  $\sim 3$  hours, 4 by  $\sim 19$  hours, and the remaining three by longer. The mean difference in time is  $15 \pm 14$  hours. The average difference in time between the hydrographic data and the EFF data was  $-4.3 \pm 4.1$  days. In locations where the velocity field was less spatially variable larger differences were allowed between the float and hydrographic data was taken. As Eulerian time-scales are generally larger than Lagrangian ones, it was acceptable to allow a few days between the CTD and the EFF measurements. The angle between the EFF trajectory and the CTD pair is  $45^\circ$  in 8 cases (averaging to  $67^\circ$ ), and is  $<45^\circ$  in 5 cases (averaging to  $11^\circ$ ). The effect of the conductivity-velocity covariance is  $<2 \text{ cm s}^{-1}$ , and is discussed further in section 5.2.1. The reference velocities used to make the geostrophic velocities absolute ranged from  $\pm 0.5 \text{ m s}^{-1}$ , with a mean of  $-0.03 \pm 0.24 \text{ m s}^{-1}$ .

Generally speaking, the most obvious test for the quality of  $\bar{u}^*$  calculations would be

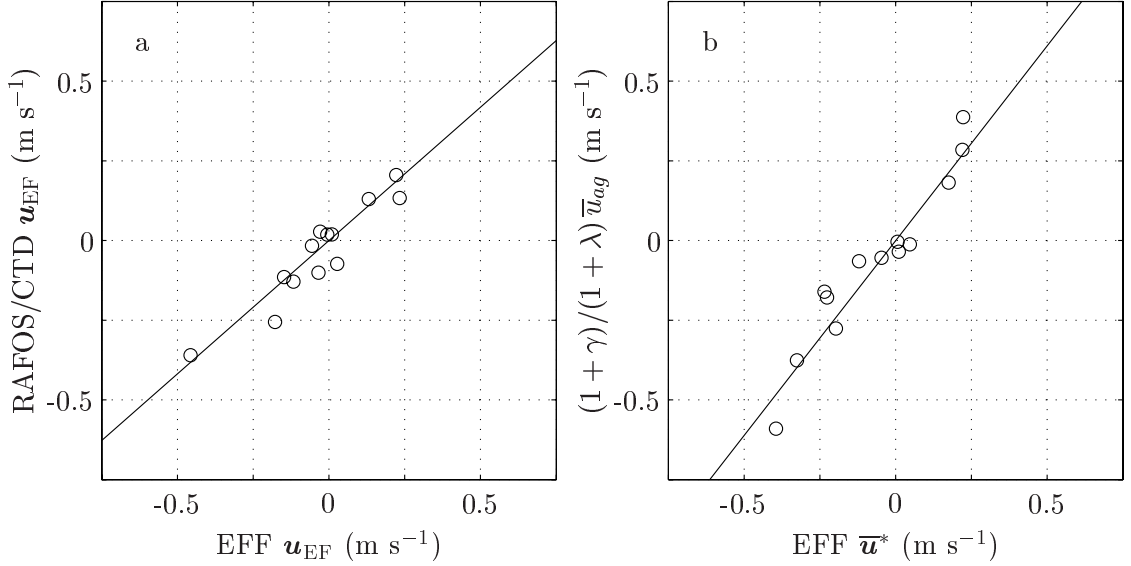


Figure 4.4: EFF data compared to absolute geostrophic velocities. (a) shows EFF  $\mathbf{u}_{\text{EF}}$  against the same quantity calculated from RAFOS and geostrophic velocities, and (b) shows EFF  $\bar{\mathbf{u}}^*$  against the same quantity calculated from RAFOS and geostrophic velocities. See text for details.

to plot EFF-derived  $\bar{\mathbf{u}}^*$  against a similar quantity calculated from absolute geostrophic velocities. Both the EFF  $\bar{\mathbf{u}}^*$  and the absolute geostrophic velocities depend on  $\mathbf{u}_{\text{RAFOS}}$ , however, and so are not independent. To obviate this concern I shall first compare two identical quantities, one derived from the EFF electromagnetic measurements and the other derived from RAFOS and hydrographic data.

The raw electric field is directly related to the electric field velocity  $\mathbf{u}_{\text{EF}}$ , which is the difference in velocity between the float and  $\bar{\mathbf{u}}^*$  (equation 2.3). The right hand side can be expressed as a combination of RAFOS and hydrographic data

$$u_{\text{EF}} = u_{\text{RAFOS}} - \bar{\mathbf{u}}^* = u_{\text{RAFOS}} - \left( \frac{1 + \gamma}{1 + \lambda} \right) \bar{u}_{\text{ag}}$$

where  $\bar{u}_{\text{ag}}$  is the absolute depth-averaged velocity calculated from the geostrophic velocity profile  $u_g(z)$

$$\bar{u}_{\text{ag}} = \bar{u}_g - u_g(z_{\text{float}}) + u_{\text{RAFOS}} .$$

The conductivity-velocity covariance  $\gamma$  is determined from the covariance of the geostrophic velocity profile and the conductivity profile, both of which have their means removed. I assume that  $\bar{u}_{ag} = \bar{u}$ , which lets  $\gamma \bar{u}_{ag} = \bar{\sigma' u'}/\bar{\sigma}$ . Combining these terms into one equation

$$u_{\text{EF}} = \frac{1}{1 + \lambda} \left( -\bar{u}_g + u_g(z_{\text{float}}) - \left. \frac{\bar{\sigma' u'}}{\bar{\sigma}} \right|_{\text{ctd}} + \lambda u_{\text{RAFOS}} \right) \quad (4.2)$$

shows that the only undetermined parameter on the right hand side is  $\lambda$ . Though I shall assume a value of 0.2, which is determined below, the analysis is not heavily dependent on this parameter.

Figure 4.4.a shows the linear regression of the two sides of equation 4.2. Error bars are not shown because they are either small or poorly defined. The electric field velocity has an error of  $<5 \text{ mm s}^{-1}$ , while that of the right has errors of  $\sim 5 \text{ mm s}^{-1}$  due to  $\lambda u_{\text{RAFOS}}/(1 + \lambda)$  in addition to uncertainties in the geostrophic calculations. Undesired synoptic processes (e.g. internal waves, geostrophic velocities) are likely to be of greater magnitude in  $u_g$  than errors in the density or pressure fields, but their effects are hard to estimate. Integrating vertically should reduce errors from internal wave and other vertically-localized perturbations.

Linear regression is significant, with a correlation coefficient of 0.94. Using different values for  $\lambda$  — a constant 0.1 or values taken from bottom sediment conductance maps of Flosadóttir et al. (1997) or Tyler et al. (1997) — still results in correlation coefficients of 0.91–0.93, justifying that the fit is independent of  $\lambda$ . These results show that the two data sets are independent of each other and that different combinations of them are justified.

It is more informative to compare the depth-averaged velocities that result from equation 4.2 (Figure 4.4.b) —  $\bar{u}^*$  and  $(1 + \gamma)/(1 + \lambda) \bar{u}_{ag}$  — however, as they are more physically meaningful. The errors in  $\bar{u}^*$  ( $2 \text{ cm s}^{-1}$ ) are not shown, while errors in the right hand side are given a lower bound by the error in  $u_{\text{RAFOS}}$  of  $2 \text{ cm s}^{-1}$ . With this form it is not necessary to assume a value for  $\lambda$ , in fact the linear regression finds its best-fit value. The two velocities are in very good agreement with each other ( $r = 0.96$ ). The slope of the fit  $(1 + \lambda)$  is  $1.22 \pm 0.10$ , or  $\lambda = 0.22 \pm 0.10$ . Unlike global oceanic models that calculate the bottom sediment conductance by making broad assumptions, this is a direct measurement of the true bottom sediment conductance.

The good fit of the two velocity data sets shows that all of the assumptions used here give accurate results, both in the theoretical description of how the oceanic electric field relates to oceanographic velocities and in the assumption that the geostrophic velocities are an accurate description of the true oceanic velocity. The rms deviation of EFF  $\bar{u}^*$  from the linear fit ( $7 \text{ cm s}^{-1}$ ) is the magnitude of terms not accounted for, whether they are noise in the measurements or neglected processes. It is a few times larger than the error in the measurements and still much smaller than the large velocities observed in the NAC.

#### 4.5 Comparison to PIES/GEM Velocities

The floats were launched along a transect that was instrumented with pressure-equipped inverted echo sounders. The time it takes for an acoustic signal to go from the sea floor to the surface and back is highly correlated with both the temperature and the specific volume anomaly ( $\delta$ ) structure of the water column — this is the gravest empirical mode (GEM) method (see Meinen and Watts, 2000). Integrating  $\delta$  vertically and differencing between PIES locations gives geostrophic velocities, which can be made absolute by data from pressure sensors and deep current meters (Meinen and Watts, 1998). Meinen and Watts (2000) kindly provided velocity data for the dates when the EFFs were launched with which to compare the EFF measured  $\bar{u}^*$  velocities. As the PIES/GEM method relies on geostrophic calculations, only one component of the velocity can be compared which will be notated as  $u$ . The velocity data were filtered with a 40 hour low-pass filter and subsampled to noon on each day.

The comparisons are shown in Table 4.1. The float's position along the array was found by the position where the bottom depth was the same as at the float's location. The PIES/GEM velocity was interpolated to the 2-D position of the float and is called  $\mathbf{u}_{\text{PIES}}(z_{\text{float}})$ . The EFFs were within 10 km of the PIES transect, except for EFF 10 at Oct 25, 1315. At the float's horizontal position along the array the PIES/GEM velocity profile was averaged vertically to obtain  $\bar{u}_{\text{PIES}}$ , and the EFFs'  $\bar{u}^*$  was multiplied by  $(1+\lambda)/(1+\gamma)$  to yield  $\bar{u}_{\text{EFF}}$ .  $\gamma$  and  $(1+\lambda)/(1+\gamma)$  were calculated when the floats where deployed 1-2

Table 4.1: Comparison between EFF and PIES/GEM velocity data (PIES/GEM data from Meinen and Watts, pers. comm., 2003). The top half contains PIES/GEM data interpolated to the locations of EFFs 7 and 10. The bottom half contains EFF data from floats 7 and 10. The parameters of direct comparison between EFF and PIES/GEM are in the same columns:  $u_{\text{PIES}}(z_{\text{float}})$  and  $u_{\text{RAFOS}}$ ;  $\bar{u}_{\text{PIES}}$  and  $\bar{u}_{\text{EFF}}$ . The distance between the EFFs and the PIES/GEM transect is given in the last column. See text for details.

date and time		$u_{\text{PIES}}(z_{\text{float}})$		$\bar{u}_{\text{PIES}}$			
(in 1994, UTC)		(m s <sup>-1</sup> )		(m s <sup>-1</sup> )			
PIES/	Oct 24, 1200	0.197	0.210	0.022	0.121		
GEM	Oct 25, 1200	0.227	0.292	0.036	0.196		
	interpolated at/from EFF:	7	10	7	10	7	10
EFF	Oct 24, 1315	0.084	—	-0.067	—	0.7	5.6
	Oct 25, 1315	0.101	0.330	-0.007	0.153	7.4	26.4
date and time		$u_{\text{RAFOS}}$		$\bar{u}_{\text{EFF}}$		distance from	
(in 1994, UTC)		(m s <sup>-1</sup> )		(m s <sup>-1</sup> )		transect (km)	

days prior to these dates: for EFF 7 they are -0.146 and 1.429, and for EFF 10 they are 0.061 and 1.149, respectively, with  $\lambda = 0.22$  as previously estimated.

The agreement between the float velocity and the PIES/GEM velocity at the float's position has an rms difference of 10 cm s<sup>-1</sup>. The deviation between the two velocities is comparable to their speeds, but note that the speeds (both  $u_{\text{RAFOS}}$  and  $\bar{u}$ ) are relatively weak. The rms deviation between the vertically averaged velocities is 6 cm s<sup>-1</sup>. Fitting the two vertically averaged velocities to a line through the origin results in a promising fit ( $m = 1.0 \pm 0.5$ ,  $r = 0.71$ ), but with only 3 data points this is not statistically significant.

Meinen (2001) shows some representative velocity transects taken from his 1.5 year deployment of PIES. Integrating them graphically gives a range of  $\bar{u}$  values ranging from 0.4 to -0.23 m s<sup>-1</sup> for a strong NAC and Mann eddy, with usual values of 0.1–0.2 m s<sup>-1</sup>. This data was taken to the south of the EFF trajectories, which is closer to the start of the NAC.

## Chapter 5

# DISCUSSION

### 5.1 *Observations*

This deployment of EFFs is the largest experiment to date of the barotropic velocity field from a Lagrangian platform. In this section  $\bar{u}^*$  is adjusted by the best estimate of the fractional bottom sediment conductance to yield  $\bar{u}_{\text{est}}$ , via  $1.22 \bar{u}^* = \bar{u}_{\text{est}}$  (see section 4.4, for unadjusted  $\bar{u}^*$  values see section 3.3).

A strong eastward branch of the NAC at  $42.5^\circ\text{N}$  advected all EFFs, though they entered it at different times and places. Strong speeds of  $0.6\text{--}0.9 \text{ m s}^{-1}$  were recorded for  $\bar{u}_{\text{est}}$ . In nearby eddies and recirculations,  $\bar{u}_{\text{est}}$  was still strong with magnitudes of  $0.25\text{--}0.35 \text{ m s}^{-1}$ . It was only in the regions away from the main current that the estimated barotropic velocity was observed below  $0.1 \text{ m s}^{-1}$ , though even in these regions fast velocities were seen intermittently. Kearns and Rossby (1998) found that in 1994 the amplitude of the trough at  $43^\circ\text{N}$  is very large, with similar positions being observed only 5% of the time over the past 80 years.

In addition to large barotropic flow the NAC is also a surface intensified current, which can be seen by comparing floats that equilibrated at different depths. The float that was closest to the surface (8) shows the greatest variability of  $\mathbf{u}_{\text{RAFOS}}$ . Its trajectory has the most abrupt changes in direction of all of the floats and is often in a different direction than the barotropic flow, and thus the ratio of the baroclinic to the barotropic component is consistently  $> 1$ . The float quickly left the region of strong flow into a region of less coherent structure. The remaining floats, all of which are deeper, moved at velocities closer to  $\bar{u}^*$ , with  $|\mathbf{u}_{\text{EF}}|/|\bar{u}^*|$  nearer to 1. The deepest float (9) moved at very close to the barotropic velocity. It is only when it slows down and leaves the main current at  $44^\circ\text{N}$   $44^\circ\text{W}$  that  $\bar{u}^*$  becomes the same order as  $\mathbf{u}_{\text{RAFOS}}$  and that  $|\mathbf{u}_{\text{EF}}|/|\bar{u}^*|$  approaches 1.

Measurements of  $\bar{u}^*$  were taken by Sanford (unpublished data) in the same region on *R/V Oceanus* cruise 259 in July 1993 using the towed transport meter (TTM) agree with the EFF observations. The TTM measures the surface horizontal electric field perpendicular to the ship track. The Mann Eddy is clearly visible at 44°W and 42°N, as are many tight recirculations and strong currents. Again, strong currents consistently reach up to 0.5 m s<sup>-1</sup>  $\bar{u}^*$ , though these observations may not be representative of the true magnitudes due to oblique crossings of the NAC. These synoptic data are remarkably similar in structure to other work, especially Rossby's cartoon of the NAC current (1996, adapted in Figure 1.1). The  $\bar{u}^*$  measurements of the EFFs in the following year are again consistent with these results, within the known time-variability of the region.

When the barotropic velocity variability is compared against that of velocities on isosurfaces, it is striking how similar they are. Previous reports have stated that they suspected or inferred significant barotropic velocities in the region — Zhang et al. (2001) from the similarity of observations on  $\sigma_\theta = 27.2$  and 27.5, Salmon (1980) from the fact that the potential energy cascade in the NAC would create barotropic velocity components, and Meinen (2001) from direct velocity calculations — that are consistent with our vertically averaged results. The barotropic velocities are smaller than the velocities observed on isopycnal or pressure surfaces (see Meinen, 2001; Zhang et al., 2001), but they both are the same order. The Eulerian average velocity of a cross-current transect over 19 months (Meinen, 2001) show that the maximum current reaches 0.6 m s<sup>-1</sup> above 500 m. Synoptic cross-sections by Meinen (2001) reveal a large variability in current structure. Barotropic velocities ( $\bar{u}$ ) are typically 0.1–0.2 m s<sup>-1</sup>, with peaks of 0.4 m s<sup>-1</sup> (toward NNE) and -0.23 m s<sup>-1</sup> (toward SSW) in a strong NAC jet and a strong recirculation that appears to be the Mann eddy, respectively. The transect is just upstream of where the EFFs were deployed heading ESE from the tail of the Grand Banks.

The EFFs were deployed in a branch of the NAC that is close to a strong and persistent recirculation, the Mann Eddy. The velocities and transports in this region may be stronger or larger than in less energetic regions of the NAC such as farther north or closer to its bifurcation from the Gulf Stream.

The loop that EFF 8 executes at 41°N 39°W (see Figure 3.6b) was investigated further because of its resemblance to a barotropic planetary Rossby wave (e.g. Price and Rossby, 1982). The float transits around the eddy in 10.5 days. The average value of all surrounding measurements of  $\bar{u}^*$  is  $(0.8, 2)$  cm s $^{-1}$  (for  $(u, v)$ , or magnitude 2 cm s $^{-1}$  and heading 22°T), which can be considered the average barotropic divergence of the eddy.

Despite no indication of the wave's spatial extent, the phase and group velocities can be calculated assuming arbitrary directions of energy propagation. Such estimates make use of the observed wave period (10.5 days) and the dispersion relation of a planetary Rossby wave under the influence of bottom topography (LeBlond and Mysak, 1978; Price and Rossby, 1982; with a bottom slope of 1 km/400 km in the 45°T direction). Regardless of the direction of energy propagation, phase velocities are larger than 0.3 m s $^{-1}$  and group velocity speeds are larger than 0.7 m s $^{-1}$ . Since the oscillation that causes the float to loop is apparent for at least 11 days, the energy that makes up the wave must pass through the region in the same amount of time. The minimum group velocity implies a spatial scale of at least 600 km. Lacking additional information about this feature, however, its nature can only be hypothesized.

### 5.1.1 Velocity Spectra

The barotropic velocity can be influenced by oscillatory motions in the ocean that arise independent of the large-scale flow, such as tidal or inertial motion. The effect of block averaging both  $\mathbf{u}_{\text{RAFOS}}$  (implicitly) and  $\mathbf{u}_{\text{EF}}$  (explicitly) over 12 hours has the potential to bias the measured spectral power. In particular for sharp peaks spectral power may leak across frequencies. Because data gaps create significant problems in calculating spectra, only the data from float 9 were used here because it was nearly continuous. The only two data points with no measurements were filled in by interpolation. Since float 9 moved at close to the barotropic velocity, the magnitude of  $\mathbf{u}_{\text{EF}}$  is small and its spectrum has smaller energy range than might be expected.

A multitaper analysis that smoothed the spectrum with a half-bandwidth of  $NW\Delta t = 2$  was performed using discrete prolate spheroidal sequences as the tapers (Percival and

Walden, 1993), where  $N$  is the length of the time series,  $\Delta t$  is the sampling interval, and  $W$  is the frequency resolution of the estimate. Taking the spectra of  $(u \mp iv)/\sqrt{2}$  gave rotary velocity spectra in the clockwise (CW) and counterclockwise (CCW) directions, respectively. The spectra of pressure,  $\mathbf{u}_{\text{RAFOS}}$ ,  $\mathbf{u}_{\text{EF}}$ , and  $\bar{\mathbf{u}}^*$  were calculated and are shown in Figure 5.1. The EF data ( $\Delta t = 4$  hours) resolve periods from 8 hours to 43 days, and the RAFOS data ( $\Delta t = 12$  hours) resolve periods of 24 hours to 43 days. All of them are red processes, with the most energy at small frequencies. The frequencies expected to have strong oscillatory motion are tidal ( $T \approx 12, 24$  hours,  $\omega \approx 0.08, 0.04$   $\text{s}^{-1}$ ) and inertial ( $T = 16.9$  hours,  $\omega = 0.059$   $\text{s}^{-1}$ ), which are either above or close to the Nyquist sampling frequency. The frequencies at which they will be aliased (for  $\Delta t = 12$  hours) were calculated for comparison:  $T \approx 350, 230, 24$  hours or  $\omega \approx 0-0.004, 0.040$   $\text{s}^{-1}$  for tidal signals; and  $T = 41$  hours or  $\omega = 0.024$   $\text{s}^{-1}$  for inertial signals. The buoyancy frequency, with a period of about 30 minutes in this region, cannot be resolved by these measurements.

There are no significant peaks in the pressure record at periods shorter than 100 days, which is what we expect: aside from buoyant oscillations none of the above processes would systematically effect the float's depth.

The energy in  $\mathbf{u}_{\text{EF}}$  at low frequencies is comparable to the peak at inertial frequencies, which is probably due to very weak  $\mathbf{u}_{\text{EF}}$  velocities. The four hour data have a sharp peak at the inertial frequency in the CW rotary component, with no peak in the CCW component, consistent with inertial waves rotating CW in the northern hemisphere. Reducing  $\mathbf{u}_{\text{EF}}$  to 12 hours by bin averaging aliases this peak to the CCW component, as well as decreasing its magnitude and leaking some power to the CW component. In both the 4-hour and 12-hour data the peaks associated with the inertial frequency are statistically significant.

The  $\mathbf{u}_{\text{RAFOS}}$  spectrum is largest at low frequencies, and there is a bump at the aliased inertial frequency 2 orders of magnitude smaller than at the lowest frequencies. This peak is not significant, however. The combination of  $\mathbf{u}_{\text{EF}}$  and  $\mathbf{u}_{\text{RAFOS}}$  yield a slightly larger peak at the inertial frequency, but it is still not very significant.

Though inertial oscillations tend to be have small vertical scales with respect to the

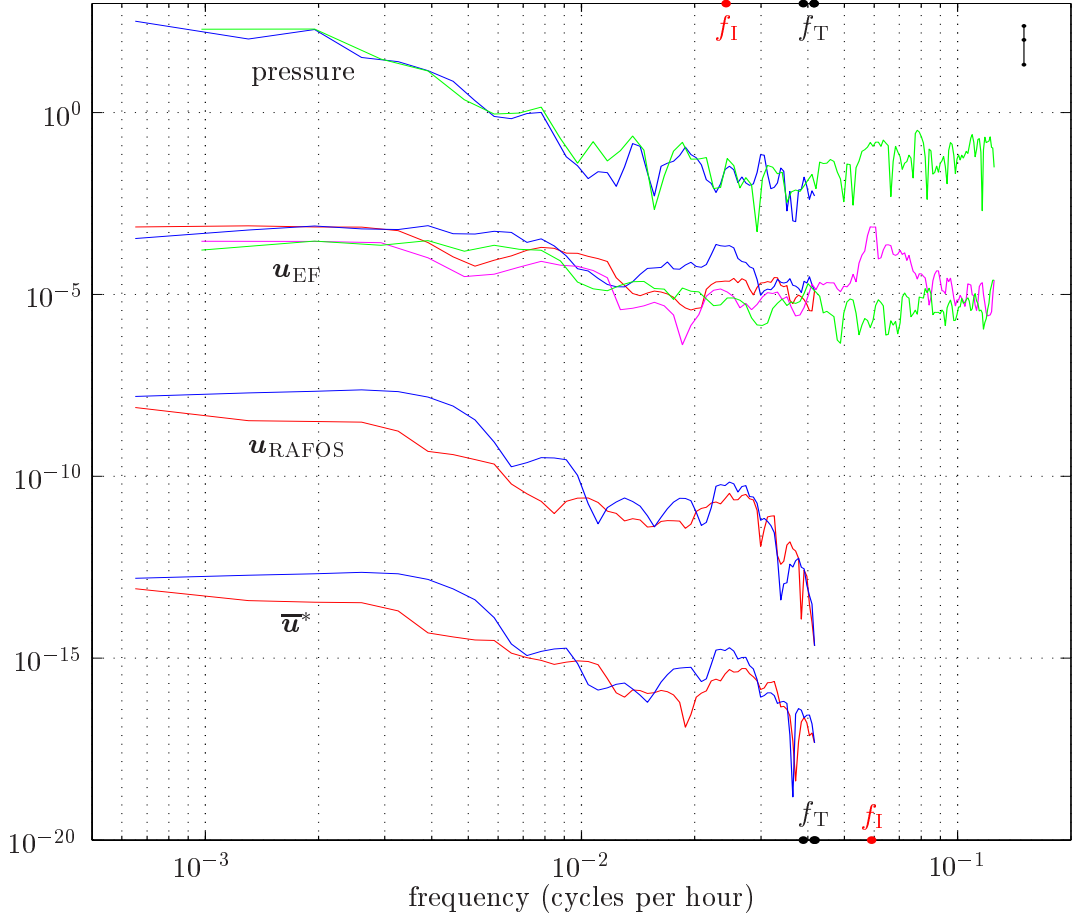


Figure 5.1: Power Spectra for pressure and velocities. The velocities are all rotary spectra, with the clockwise component in red and the counterclockwise component in blue for velocity data taken every 12 hours. From top to bottom are: pressure every 4 hours (green) and averaged every 12 hours (blue);  $u_{EF}$  every 4 hours (magenta: CW; green: CCW) and averaged every 12 hours;  $u_{RAFOS}$  every 12 hours; and  $\bar{u}^*$  every 12 hours. All spectra are normalized by their variance (in parentheses): pressure every 4 hours ( $1.35 \times 10^3$  dbar $^2$ ) and every 12 hours ( $1.24 \times 10^3$  dbar $^2$ );  $u_{EF}$  every 4 hours ( $1.59 \times 10^{-3}$  m $^2$  s $^{-2}$ ) and every 12 hours ( $6.00 \times 10^{-3}$  m $^2$  s $^{-2}$ );  $u_{RAFOS}$  every 12 hours ( $3.83 \times 10^{-2}$  m $^2$  s $^{-2}$ ); and  $\bar{u}^*$  every 12 hours ( $3.86 \times 10^{-2}$  m $^2$  s $^{-2}$ ). The variances are taken of the complex velocity  $\mathbf{z} = u + iv$ . The groups of spectra are offset by factors of 1,  $10^{-5}$ ,  $10^{-10}$ , and  $10^{-15}$  from top to bottom. The dots on the x-axes show the inertial frequency (red,  $f_I$ ) and selected tidal frequencies (black, for the O<sub>1</sub>, P<sub>1</sub>, and K<sub>1</sub> constituents,  $f_T$ ), with those at the bottom of the figure being the direct frequencies that are fully resolved by the 4-hour data and those at the top being for the aliased and direct frequencies that are resolved by the 12-hour data. The line in the top right shows the 95% confidence intervals. See the text for more detail.

depth of the water column in the open ocean, these signals are apparent in the depth averaged data. This may be due to poor spectral properties of the sampling scheme (block averaging) in addition to the very small magnitudes of  $\mathbf{u}_{\text{EF}}$ .

The coherence cross-spectrum between  $\mathbf{u}_{\text{EF}}$  and  $\mathbf{u}_{\text{RAFOS}}$  (not shown) shows that the two signals are only coherent at high frequencies. Peaks in the coherence occur at periods of 30, 26, and above 24 hours. The latter two peaks are close to the expected periods (whether aliased or direct) of the  $O_1$  or the  $P_1$  and  $K_1$  tidal constituents.

## 5.2 Calibration Factors

The previous chapter presented comparisons with independent velocity data sets to show that the velocity calculated by the EFFs is consistent with other techniques. In this section I shall discuss how the parameters estimated there relate to oceanographic conditions and previous studies.

### 5.2.1 Velocity-Conductivity Covariance

The velocity-conductivity covariance calculated in section 4.4 from geostrophic velocity and conductivity profiles is shown in Figure 5.2; it is the fraction by which  $\bar{\mathbf{u}}^*$  is different from  $\bar{\mathbf{u}}$  due to baroclinic structure in the water column. Note that although the sign of  $\bar{\mathbf{u}}$  is arbitrary and depends on the orientation of the two hydrographic stations, the sign of  $\gamma$  is significant, showing whether velocity and conductivity are positively or negatively correlated. Though  $\gamma$  can be as large as  $\pm 0.5$ , what is more important is the magnitude of the correction to  $\bar{\mathbf{u}}$ . Multiplying by  $\bar{\mathbf{u}}$  gives the correction in  $\text{m s}^{-1}$ , or  $\bar{\sigma}'\bar{\mathbf{v}}'/\bar{\sigma}$ . This dimensional value is seen to be smaller than  $2 \text{ cm s}^{-1}$  in all cases, since large values tend to occur for small  $\bar{\mathbf{u}}$ . Because  $\gamma\bar{\mathbf{u}}$  does not depend on knowledge of an absolute velocity profile, it can also be calculated from other pairs of hydrographic data in the survey. It was found to be  $< 2 \text{ cm s}^{-1}$  in regions close to the axis of the NAC, while outside it was  $5 \text{ mm s}^{-1}$  or smaller. The error due to  $\gamma$  is the same magnitude as other errors in the velocity data.

These results are consistent with those of Chave and Luther (1990), which is surprising

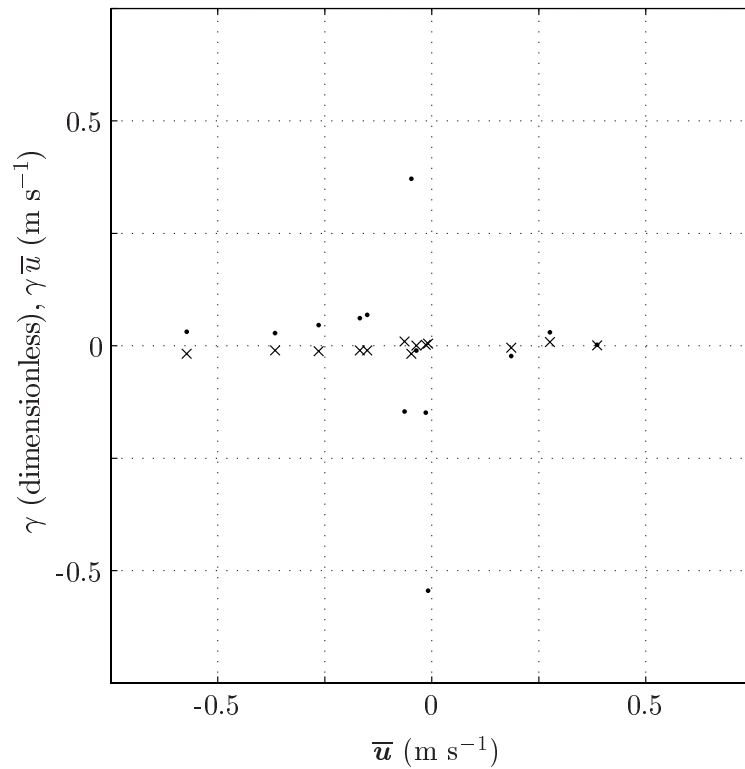


Figure 5.2: Velocity-conductivity covariance calculated from absolutely referenced geostrophic velocity profiles and hydrographic data (see section 4.4 for details).  $\gamma$  is shown by  $\bullet$ , and  $\gamma \bar{u} = \bar{\sigma}' \bar{u}' / \bar{\sigma}$  by  $\times$ .

given that our measurements are in a surface intensified western boundary current. Using zonally averaged ocean property profiles, Chave and Luther (1990) found that the first baroclinic mode in the Atlantic has only a few percent effect on  $\bar{u}^*$ . Furthermore, using results from POLYMODE they show that the first baroclinic effect is 7–9% of that of the barotropic mode. In our data, with the effects of baroclinicity being less than  $2 \text{ cm s}^{-1}$  and with speeds of  $\bar{u}$  being  $0.25\text{--}0.6 \text{ m s}^{-1}$ , the effect of baroclinic structure is 3–8% of the depth-averaged velocity.

### 5.2.2 Bottom Sediment Conductance

The value of  $\lambda$  can also be calculated from the known sediment distribution. Using a geologically realistic 1-dimensional conductance model for the open Atlantic, Chave and Luther (1990) found that this factor is likely to be spatially constant and to be from 0–0.1 for signals over a wide range of frequency and wavenumber space. From a global circulation and electromagnetic model with  $1^\circ$  resolution that uses observed sediment thicknesses, (Tyler, personal communication, 2003) calculated  $\lambda$  to be 0.02–0.1 in the deployment region. There is a strong gradient of  $\lambda$  along the continental slope due to thickening sediment layers closer to the continental shelf. An electromagnetic model of the North Atlantic by Flosadóttir et al. (1997), also with  $1^\circ$  resolution, found similar variability for  $\lambda$ , though the magnitudes were 0.06–0.2.

The numerous assumptions and uncertainties in the sediment conductance of these models can be contrasted with direct observations made by the comparison in section 4.4. When comparing the EFF  $\mathbf{u}_{\text{EF}}$  to the same quantity calculated from RAFOS and hydrographic data (Figure 4.4a), varying the value used for lambda gave very similar results. The values tried were 0.1, 0.22, and interpolations from the maps of  $\lambda$  calculated by Flosadóttir et al. (1997) and Tyler et al. (1997). Though the results were statistically indistinguishable, with  $r$ -values of about 0.93, the best fit was obtained with a value of 0.22. As mentioned earlier, the best estimate for  $\lambda$  ( $0.2 \pm 0.1$ ) is used to relate  $\bar{u}^*$  to  $\bar{u}$  throughout this paper, unless noted otherwise.

### 5.2.3 Non-Local Currents

In the initial presentation of theory, effects of non-local currents ( $\mathbf{J}^*$ ) were neglected because they are usually small in magnitude and cannot be resolved by EFFs. As shown in section 4.4, the simplified theory is in error compared to the absolute geostrophic velocities by less than the rms deviation ( $7 \text{ cm s}^{-1}$ ), though part of this is expected to be from measurement noise in the EFF and geostrophic techniques. The values of  $\mathbf{J}^*$  can be given the same upper limit from the rms deviations of the fit to absolute geostrophic velocities.

Non-oceanic signals can also arise from atmospheric disturbances of the magnetic field. Magnetotelluric storms typically have very large (global) length scales and have fluctuations at periods smaller than 2 days. A measure of the magnitude of variations in the horizontal magnetic field is given by the K-index, which is recorded every three hours. It is a logarithmic scale, on which values greater than 4 indicate magnetotelluric storms. K-index values during the EFF deployment are shown in Figure 5.3. Though there are a few peaks above 4 when averaged over 12 hours, they never last for more than one day.

Averaging EFF data every 2 days or filtering them with a low-pass filter with a cut-off at 2 days would be the best way to reduce non-oceanic contamination of the EF data, though at great expense to its resolution in time. In Sanford et al. (1995), which discusses EFF data from the California Current System, the  $\bar{\mathbf{u}}^*$  measurements are averaged every 2 days to remove any extra-oceanic signals. The weak and slowly varying flow off of California gives greater importance to reducing contamination of the EF velocity by atmospheric magnetic fields for accurate measurements of  $\bar{\mathbf{u}}^*$ . In the NAC region, however, the magnitudes and time scales of flow are  $>0.2 \text{ m s}^{-1}$  and  $\sim 2$  days, which make it undesirable to average the velocities over such times.

Figure 5.3 also shows the standard deviation of the electric field measured by EFFs. These are values calculated in the 4-hour averaging cycle of the EF system, which are further averaged onto the 12-hour RAFOS times and then averaged over the four floats. They are converted to a velocity (in  $\text{cm s}^{-1}$ ). For the first 10 days there is good correlation, but after that the time series are poorly correlated. Over the whole series the correlation

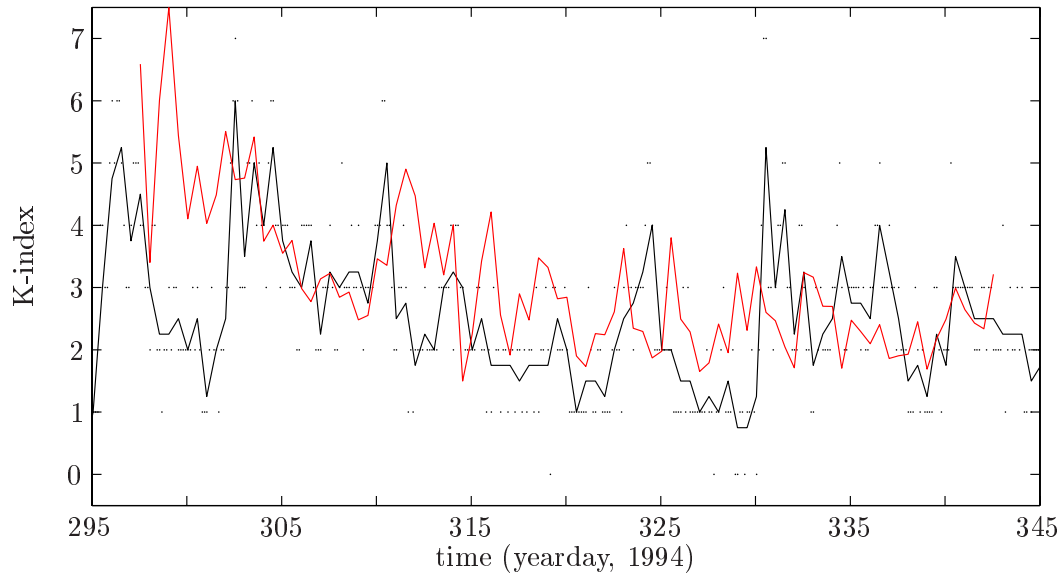


Figure 5.3: K-index values every 3 hours (dots) and averaged every 12 hours (solid line), and the standard deviation of  $u_{EF}$  averaged every 12 hours (red,  $\text{cm s}^{-1}$ ). The K-index is a logarithmic quantity related to the variation of the horizontal component of the earth's magnetic field.

coefficient is 0.25, so the K-index accounts for 6% of the amplitude of the variance of the standard deviation. Further disincentive for filtering or averaging  $\bar{\mathbf{u}}^*$  over longer periods is that the atmospheric variability of  $\mathbf{u}_{\text{EF}}$  ( $2\text{--}4 \text{ cm s}^{-1}$ ) is the same magnitude as other errors.

### 5.3 Dynamics

#### 5.3.1 Integral Scales

The autocorrelation sequence of  $\bar{\mathbf{u}}^*$  gives information about how quickly the turbulent structure of the flow varies.

The many data gaps in the velocities complicate finding autocorrelation sequences so standard techniques could not be used. A convolution in the time domain was taken between all valid data points. Regardless of how many terms were in the convolution sum at each lag, I divided by the length of the total sequence  $N$ . This is in analogy to the ‘biased’ estimate of the autocorrelation sequence (Percival and Walden, 1993) that accounts for reduced certainty at large lags by decreasing its value by  $1/N$  instead of  $1/(N - |\tau|)$ , making the result more statistically robust. The autocorrelation sequence was then averaged across floats. The autocorrelation sequences are shown in Figure 5.4. The integral time-scale  $\Gamma$  and integral length-scale ( $L$ ) are defined as (Taylor, 1921)

$$\Gamma = \int_0^{\tau_0} r(\tau') \, d\tau' \quad \text{and} \quad L = \Gamma \left( \overline{u'^2} \right)^{1/2}$$

where  $\tau_0$  is the first zero-crossing of  $r(\tau)$  and the components of  $\bar{\mathbf{u}}^*$  are used for the velocity. The theory used to calculate this assumes that the flow field is stationary, homogeneous, without any mean flow, and that the particles are advected by the velocity of interest. Though these cases are clearly overly restrictive in most oceanographic regions, it is common to use these equations even if there is a mean background velocity with strong spatial variability (e.g. Bracco et al., 2000; LaCasce and Bower, 2000).

The integral time-scales of  $\bar{\mathbf{u}}^*$  are  $1.6 \pm 0.4$  and  $1.3 \pm 0.4$  days for  $\bar{u}^*$  and  $\bar{v}^*$ , respectively, with corresponding length-scales of  $28 \pm 8$  and  $15 \pm 5$  km. The errors in  $\Gamma$  are due to

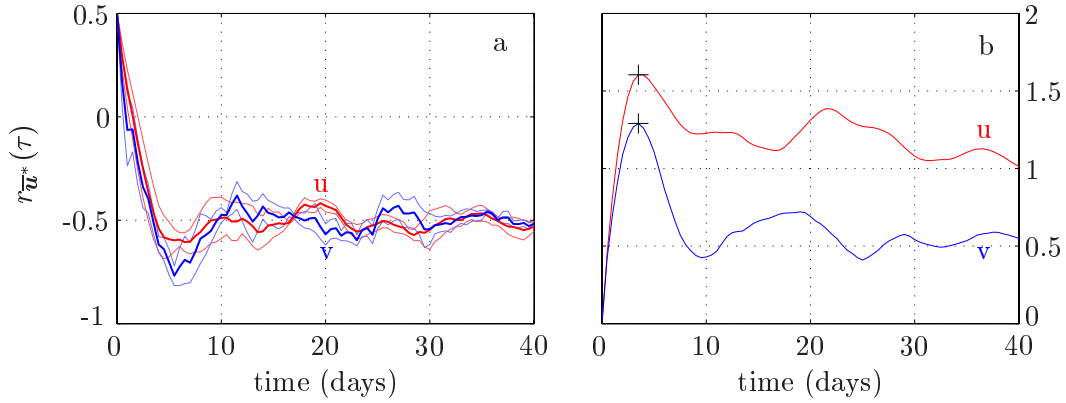


Figure 5.4: Autocorrelation sequence of  $\bar{u}^*$  (red) and  $\bar{v}^*$  (blue) (a), with the 95% confidence limits given by the light-colored lines, and the cumulative integral of the autocorrelation sequences (b), with the integral time-scales marked by a black +. See text for details.

uncertainty in  $r$ , and errors in  $L$  are due to those in  $\Gamma$  and in  $(\overline{u'^2})^{1/2}$ .

To gain a point of comparison I calculated similar scales for  $\mathbf{u}_{\text{RAFOS}}$ , obtaining  $\Gamma$  of  $2.0 \pm 0.3$  and  $1.6 \pm 0.2$  days for  $u_{\text{RAFOS}}$  and  $v_{\text{RAFOS}}$ , respectively, and  $L$  of  $53 \pm 12$  and  $28 \pm 6$  km. These values are consistent with those that Zhang et al. (2001) calculated,  $\Gamma = 2.2$  days and  $L = 28$  km, and furthermore give us confidence that despite not removing the mean velocity field in  $1/2^\circ$  bins like they did our results are not greatly affected. The time-scales for  $\mathbf{u}_{\text{RAFOS}}$  are slightly larger than those for  $\bar{u}^*$ , just on the edge of being significant. This makes sense, because barotropic motions have shorter response times than baroclinic motions. The variability of  $\bar{u}^*$  (or  $\bar{u}$ ) and that of  $\mathbf{u}_{\text{RAFOS}}$  are very similar, aside from the fact that  $\bar{u}^*$  is of smaller magnitude.

### 5.3.2 Transport

Though these observations were not collected with the goal of calculating transports, and the deployments were not planned to accomplish this, it is still possible to extrapolate possible transport values. I shall only calculate values for the strong eastward flowing branch that was seen at roughly  $42.5^\circ\text{N}$ . This feature was observed by all of the floats and is persistent enough to be addressed here.

The EFF data, though they cover the length of this eastward branch of the NAC, do not show much about the cross-section of the current. Observations from the literature give its width as 100 km or larger (Kearns and Rossby, 1998; Meinen, 2001; Zhang et al., 2001) and its velocity cross section as triangular to a first approximation (Meinen, 2001; Zhang et al., 2001). I take the peak velocity as  $0.6 \text{ m s}^{-1} \bar{\mathbf{u}}$  ( $0.5 \text{ m s}^{-1} \bar{\mathbf{u}}^*$ ). Though this is not the maximal speed observed, it has been observed consistently by EFFs and by other EM observations and is not anomalous. These assumptions together with the known depth yield a transport of 140 Sv. Recent studies using absolute geostrophic velocities and PIES/GEM velocities measured nearby and in the same year give transports that are in a similar range, from 110-140 Sv (Meinen, 2001; Meinen and Watts, 2000).

A second but less direct way to estimate the volume transport is to use Zhang et al.'s (2001) map of the mean velocity field on isopycnal surfaces. From a subset of EFF data that is within the eastward jet ( $42.4\text{--}43^\circ\text{N}$   $42\text{--}46^\circ\text{W}$ ) I form an average vertical profile of  $|\bar{\mathbf{u}}^*|/|\mathbf{u}_{\text{RAFOS}}|$ . Since  $\bar{\mathbf{u}}^*$  and  $\mathbf{u}_{\text{RAFOS}}$  always point in the same direction, averaging to  $0 \pm 10^\circ$  for each float's data, the ratio of the magnitudes are sufficient for converting between  $\mathbf{u}_{\text{RAFOS}}$  and  $\bar{\mathbf{u}}^*$ . Interpolating  $|\bar{\mathbf{u}}^*|/|\mathbf{u}_{\text{RAFOS}}|$  to the mean depth of the  $\sigma_\theta = 27.5$  isopycnal and multiplying by the mean velocity field yields a spatial map of  $\bar{\mathbf{u}}^*$ . The mean velocity field from Zhang et al. (2001) is very robust, formed over a two year period with  $\geq 40$  data points in each  $1/2^\circ$  by  $1/2^\circ$  bin. The vertical profile of  $|\bar{\mathbf{u}}^*|/|\mathbf{u}_{\text{RAFOS}}|$  is much less so, however, there are essentially 4 data points that correspond to each of the 4 floats. The resulting velocity map is averaging zonally onto a N-S transect at  $44^\circ\text{W}$ . The width of the NAC is 170 km between points that are  $1/e$  of the maximum velocity, with a corresponding transport of 360 Sv (or 440 Sv correcting for  $\lambda$ ). This seems unreasonably large, and could result from the very large meander in late 1994 that biases the vertical structure of  $|\bar{\mathbf{u}}^*|/|\mathbf{u}_{\text{RAFOS}}|$ .

## Chapter 6

### SUMMARY

The Electric Field Float was built to measure barotropic velocity from a Lagrangian subsurface float. It is a RAFOS float with additional components that measure the ambient electric field. To obtain high quality measurements angled vanes cause it to rotate about its vertical axis due to internal waves and other vertical water processes. Every four hours internal processing demodulates the oceanic electric field and averages measurements of rotation, temperature, and pressure. Position fixes from RAFOS tracking occur every 12 hours, from which float velocities are calculated by centered differencing. Block averaging  $\mathbf{u}_{\text{EF}}$  onto the times of RAFOS fixes and combining with  $\mathbf{u}_{\text{RAFOS}}$  yields the conductivity-weighted depth-averaged velocity  $\bar{\mathbf{u}}^*$ . This variable is related to the barotropic velocity ( $\bar{\mathbf{u}}$ ), which I define as the vertical average of the absolute velocity profile, by two multiplicative factors: the vertical covariance between electrical conductivity and velocity ( $\gamma$ ), and the fraction of bottom sediment conductance to water column conductance ( $\lambda$ ).

Four floats were deployed in the North Atlantic during the fall of 1994 in an eastward flowing branch of the NAC. The uncertainty in measurements of  $\bar{\mathbf{u}}^*$  is determined by an error analysis, by comparing pairs of measurements, and by calibration with an independent velocity data set. Hydrographic data taken during and after deployment permit validation of the electromagnetic technique through calculation of absolute geostrophic velocities.

From an error analysis we expect  $\bar{\mathbf{u}}^*$  to have an error of  $2 \text{ cm s}^{-1}$ . Pairs of measurements made by different floats show that the observed error for each measurement is  $\leq 2 \text{ cm s}^{-1}$  for measurements at the same location and taken no more than one day apart, though the oceanic variability needed for this calculation is not well resolved. Comparisons with geostrophic velocity were made when a float passed between two hydrographic profiles. The velocity of the float was used as a reference to make the geostrophic velocity

profiles absolute. The  $\bar{\mathbf{u}}^*$  observations are in good agreement with the absolute geostrophic velocities by the theoretical linear relation ( $r=0.96$ ), which shows that the electromagnetic technique gives results consistent with other techniques.

The comparison with absolute geostrophic velocities gives insight into the magnitude of various factors. The slope of the linear regression is caused by conducting bottom sediment, and yields  $\lambda = 0.22 \pm 0.10$ . This is in agreement with previously observed values (0–0.2) and with model results (0.06–0.2, Flosadóttir et al., 1997; and 0.02–0.1, Tyler et al., 1997). Though the baroclinic effects of  $\gamma$  were included in the regression, the absolute magnitude of its effect is  $< 2 \text{ cm s}^{-1}$  and is much smaller than the signal strength. The rms deviation of  $\bar{\mathbf{u}}^*$  from the best fit ( $7 \text{ cm s}^{-1}$ ) is an upper limit on all other processes that are not resolved, such as terms considered insignificant in the theory, atmospheric magnetic field variability, oceanic variability, and errors in the geostrophic velocities. To convert to an estimated  $\bar{\mathbf{u}}$ , notated  $\bar{\mathbf{u}}_{\text{est}}$ ,  $\bar{\mathbf{u}}^*$  is scaled by the slope of the linear regression ( $1 + \lambda = 1.22$ ).

Fast barotropic velocities of  $0.6\text{--}0.9 \text{ m s}^{-1}$   $\bar{\mathbf{u}}_{\text{est}}$  ( $0.5\text{--}0.75 \text{ m s}^{-1}$   $\bar{\mathbf{u}}^*$ ) were observed in the current, with nearby eddy velocities of  $0.25\text{--}0.35 \text{ m s}^{-1}$   $\bar{\mathbf{u}}_{\text{est}}$  ( $0.3\text{--}0.5 \text{ m s}^{-1}$   $\bar{\mathbf{u}}^*$ ). In the regions away from the mean location of the NAC  $\bar{\mathbf{u}}_{\text{est}}$  was typically  $0.12 \text{ m s}^{-1}$  ( $0.1 \text{ m s}^{-1}$   $\bar{\mathbf{u}}^*$ ), though speeds of up to  $0.5 \text{ m s}^{-1}$   $\bar{\mathbf{u}}_{\text{est}}$  ( $0.4 \text{ m s}^{-1}$   $\bar{\mathbf{u}}^*$ ) were intermittently seen. The ratio of the baroclinic velocity to the barotropic velocity showed the vertical structure of the current: at a depth of 150 dbar the velocities are predominantly baroclinic, at 500 dbar they are roughly equal, and at 900 dbar they are close to barotropic.

The autocorrelation of  $\bar{\mathbf{u}}^*$  gives an indication of the time variability of the  $\bar{\mathbf{u}}^*$  velocity field. The integral time-scale for  $(\bar{u}^*, \bar{v}^*)$  is  $(1.6 \pm 0.4, 1.3 \pm 0.4)$  days, and the integral length-scale is  $(28 \pm 8, 15 \pm 5)$  km. The time-scales are slightly smaller than for  $(u_{\text{RAFOS}}, v_{\text{RAFOS}})$ , which are  $(2.0 \pm 0.3, 1.6 \pm 0.2)$ . The latter scales agree with those calculated by Zhang et al. (2001), providing confidence that the 4 floats are representative of the mean flow field. The length-scale of  $u_{\text{RAFOS}}$  is roughly twice as large as calculated by Zhang et al. (2001), though that of  $v_{\text{RAFOS}}$  is the same, giving indication that the strong but unresolvable mean velocity field is influencing the length-scales in an anisotropic fashion.

The variability of the near-barotropic velocity is very similar to velocities on isopycnals.

Transport can be estimated by taking values of the spatial structure of the NAC from the literature. With a width of 100 km and a triangular velocity cross-section, transports in the current reach 140 Sv for peak speeds of  $0.6 \text{ m s}^{-1}$   $\bar{u}_{\text{est}}$  ( $0.5 \bar{u}^*$ ). Such speeds were seen consistently in the flow and are not anomalies for this time period. Recently reported absolute transports are consistent with our results.

## BIBLIOGRAPHY

Anderson-Fontana, S., M. Prater and H. T. Rossby, 1996: RAFOS float data report of the North Atlantic current study 1993-1995. Tech. Rep. 96-4, Graduate School of Oceanography, University of Rhode Island, 241 pp.

Arevalo, A., R. M. Souto and M. C. Arevalo, 1985: Preparation and reproducibility of a thermal silver-silver chloride electrode. *Journal of Applied Electrochemistry*, **15**(5), 727-735.

Babiano, A., C. Basdevant, P. Le Roy and R. Sadourny, 1990: Relative dispersion in two-dimensional turbulence. *Journal of Fluid Mechanics*, **214**, 535-557.

Boebel, O. and C. Barron, 2003: A comparison of in-situ float velocities with altimeter derived geostrophic velocities. *Deep-Sea Research II*, **50**(1), 119-139.

Bracco, A., J. H. LaCasce and A. Provenzale, 2000: Velocity probability density functions for oceanic floats. *Journal of Physical Oceanography*, **30**(3), 461-474.

Carr, M.-E. and T. H. Rossby, 2001: Pathways of the North Atlantic Current from surface drifters and subsurface floats. *Journal of Geophysical Research*, **106**(C3), 4405-4419.

Chave, A. D. and D. S. Luther, 1990: Low-frequency, motionally induced electromagnetic fields in the ocean: 1. Theory. *Journal of Geophysical Research*, **95**(C5), 7185-7200.

Clarke, R. A., 1994: Cruise report *Hudson* 94030: Newfoundland Basin. unpublished report.

Clarke, R. A., H. W. Hill, R. F. Reiniger and R. F. Warren, 1980: Current system south and east of the Grand Banks of Newfoundland. *Journal of Physical Oceanography*, **10**(1), 25-65.

Dutkiewicz, S., L. Rothstein and T. H. Rossby, 2001: Pathways of cross-frontal exchange in the North Atlantic Current. *Journal of Geophysical Research*, **106**(C11), 26917-26928.

Er-El, J. and R. L. Peskin, 1981: Relative diffusion of constant-level balloons in the southern hemisphere. *Journal of the Atmospheric Sciences*, **38**(10), 2264-2274.

Flosadóttir, Á. H., J. C. Larsen and J. T. Smith, 1997: Motional induction in North Atlantic circulation models. *Journal of Geophysical Research*, **102**(C5), 10353-10372.

Gascard, J.-C., 1973: Vertical motions in a region of deep water formation. *Deep-Sea Research I*, **20**(11), 1011-1027.

Hogg, N. G., 1992: On the transport of the Gulf Stream between Cape Hatteras and the Grand Banks. *Deep-Sea Research, Part A*, **39**(7-8A), 1231-1246.

Johns, W. E., T. J. Shay, J. M. Bane and D. R. Watts, 1995: Gulf Stream structure, transport, and recirculation near 68°W. *Journal of Geophysical Research*, **100**(C1), 817-838.

Kearns, E. J. and T. H. Rossby, 1998: Historical position of the North Atlantic Current. *Journal of Geophysical Research*, **103**(C8), 15509-15524.

König, H., K. L. S. Tokos and W. Zenk, 1991: MAFOS — a simple tool for monitoring the performance of RAFOS sound sources in the ocean. *Journal of Atmospheric and Oceanic Technology*, **8**(5), 669–676.

Krauss, W., E. Fahrbach, A. Aitsam, J. Elken and P. Koske, 1987: the North Atlantic Current and its associated eddy field southeast of the Flemish Cap. *Deep-Sea Research*, **34**(7), 1163–1185.

Krauss, W., R. H. Käse and H.-H. Hinrichsen, 1990: The branching of the Gulf Stream southeast of the Grand Banks. *Journal of Geophysical Research*, **95**(C8), 13089–13103.

LaCasce, J. H. and A. Bower, 2000: Relative dispersion in the subsurface North Atlantic. *Journal of Marine Research*, **58**(6), 863–894.

Lazier, J., 1994: Observations in the Northwest Corner of the North Atlantic Current. *Journal of Physical Oceanography*, **24**(7), 1449–1463.

LeBlond, P. H. and L. A. Mysak, 1978: *Waves in the Ocean*. Elsevier Scientific Publishing Company, New York, 602 pp.

Lherminier, P. D., 1998: *Convection profonde en Mer du Groenland: Étude expérimentale des phases de préconditionnement et de mélange*. Ph.D. thesis, Université Paris 6.

Longuet-Higgins, M. S., M. E. Stern and H. Stommel, 1954: The electrical fields induced by ocean currents and waves, with applications to the method of towed electrodes. *Papers in Physical Oceanography and Meteorology* **13**(1), Woods Hole Oceanographic Institution/Massachusetts Institute of Technology, 37 pp.

Luther, D. S., J. H. Filloux and A. D. Chave, 1991: Low-frequency, motionally induced electromagnetic fields in the ocean: 2. Electric field and eulerian current comparison. *Journal of Geophysical Research*, **96**(C7), 12797–12814.

Mann, C. R., 1967: The termination of the Gulf Stream and the beginning of the North Atlantic Current. *Deep-Sea Research*, **14**, 337–359.

Meinen, C. S., 2001: Structure of the North Atlantic current in stream-coordinates and the circulation in the Newfoundland Basin. *Deep-Sea Research I*, **48**(7), 1553–1580.

Meinen, C. S. and D. R. Watts, 1998: Calibrating inverted echo sounders equipped with pressure sensors. *Journal of Atmospheric and Oceanic Technology*, **15**(6), 1339–1345.

Meinen, C. S. and D. R. Watts, 2000: Vertical structure and transport on a transect across the North Atlantic current near 42°N: Time series and mean. *Journal of Geophysical Research*, **105**(C9), 21869–21891.

Meinen, C. S., D. R. Watts and R. A. Clarke, 2000: Absolutely referenced geostrophic velocity and transport on a section across the North Atlantic current. *Deep-Sea Research I*, **47**(2), 309–322.

Meteorological Service of Canada, National Archives and Data Management Branch, 2002: *National Climate Data and Information Archive [online database]*. Environment Canada, Gatineau, Quebec, Canada, updated July 24, 2003; cited March 24, 2004, available from: [http://www.climate.weatheroffice.ec.gc.ca/climateData/canada\\_e.html](http://www.climate.weatheroffice.ec.gc.ca/climateData/canada_e.html).

Munk, W., 1981: *Evolution of Physical Oceanography*. Chap. Internal Waves and Small-Scale Processes, pp. 263–291. Massachusetts Institute of Technology Press.

Percival, D. B. and A. T. Walden, 1993: *Spectral Analysis for Physical Applications*. Cambridge University Press, 583 pp.

Price, J. F. and H. T. Rossby, 1982: Observations of a barotropic planetary wave in the western North Atlantic. *Journal of Marine Research*, **40**(supplement), 543–558.

Reiniger, R. F. and R. A. Clarke, 1975: Circulation pattern in the Newfoundland Ridge area, 1972. in *Symposium on environmental conditions in the Newfoundland Grand Bank area in 1972 and their effect on fishery trends*, Vol. 10, pp. 57–67. International Commission for the Northwest Atlantic Fisheries, Dartmouth, Canada.

Rossby, T. H., 1996: The North Atlantic Current and surrounding waters: at the crossroads. *Reviews of Geophysics*, **34**(4), 463–481.

Salmon, R., 1980: Baroclinic instability and geostrophic turbulence. *Geophysical and Astrophysical Fluid Dynamics*, **15**(3–4), 167–211.

Sanford, T. B., 1971: Motionally induced electric and magnetic fields in the sea. *Journal of Geophysical Research*, **76**(15), 3476–3492.

Sanford, T. B., 1986: Recent improvements in ocean current measurement from motional electric fields and currents. *Proceedings of the IEEE Working Conference on Current Measurement*, **3rd**, 65–76.

Sanford, T. B., R. G. Drever and J. H. Dunlap, 1978: A velocity profiler based on the principles of geomagnetic induction. *Deep-Sea Research*, **25**(2), 183–210.

Sanford, T. B., R. G. Drever and J. H. Dunlap, 1985: An acoustic doppler and electromagnetic velocity profiler. *Journal of Atmospheric and Oceanic Technology*, **2**(2), 110–124.

Sanford, T. B., R. G. Drever and J. H. Dunlap, 1995: Barotropic ocean velocity observations from an Electric Field Float, a modified RAFOS float. *Proceedings of the IEEE Working Conference on Current Measurement*, **5th**, 163–168.

Sanford, T. B., J. H. Dunlap, J. Verrall, T. J. Osse, R. G. Drever, A. C. Bartlett and M. D. Allison, 1993: The electric field float and its sea test on R/V *Endeavor* cruise 230. Tech. Rep. 9314, Applied Physics Lab, University of Washington, 41 pp.

Sanford, T. B. and R. E. Flick, 1975: On the relationship between transport and motional electric potentials in broad, shallow currents. *Journal of Marine Research*, **33**(1), 123–139.

Schmitz, Jr., W. J. and M. S. McCartney, 1993: On the North Atlantic circulation. *Reviews of Geophysics*, **31**(1), 29–49.

Smith, W. H. F. and D. T. Sandwell, 1997: Global seafloor topography from satellite altimetry and ship depth soundings. *Science*, **277**(5334), 1957–1962.

Taylor, G. T., 1921: Diffusion by continuous movement. *Proceedings of the London Mathematical Society, Series A*, **20**, 196–221.

Tucholke, B. E., 1986: *The Western North Atlantic Region*. Chap. Structure of Basement and Distribution of Sediments in the Western North Atlantic Ocean, pp. 331–340. Geological Society of America, Inc.

Tyler, R. H., L. A. Mysak and J. M. Oberhuber, 1997: Electromagnetic fields generated by a 3-D global ocean circulation. *Journal of Geophysical Research*, **102**(C3), 5531–5551.

Voorhis, A. D., 1968: Measurements of vertical motion and the partition of energy in the New England slope water. *Deep-Sea Research I*, **15**, 599–608.

Voorhis, A. D., 1971: Response characteristics of the neutrally buoyant float. Technical Report 71-73, Woods Hole Oceanographic Institution, 75 pp.

Webb, D. C. and L. V. Worthington, 1968: Measurements of vertical water movement in the Cayman Basin. *Deep-Sea Research*, **15**, 609–612.

Worthington, L. V., 1976: On the North Atlantic circulation. *Johns Hopkins Oceanographic Studies* 6, Johns Hopkins University, 110 pp.

Zhang, H.-M., M. D. Prater and H. T. Rossby, 2001: Isopycnal lagrangian statistics from the North Atlantic current RAFOS float observations. *Journal of Geophysical Research*, **106**(C7), 13817–13836.

<b>REPORT DOCUMENTATION PAGE</b>			<i>Form Approved OPM No. 0704-0188</i>
<p>Public reporting burden for this collection of information is estimated to average 1 hour per response, including the time for reviewing instructions, searching existing data sources, gathering and maintaining the data needed, and reviewing the collection of information. Send comments regarding this burden estimate or any other aspect of this collection of information, including suggestions for reducing this burden, to Washington Headquarters Services, Directorate for Information Operations and Reports, 1215 Jefferson Davis Highway, Suite 1204, Arlington, VA 22202-4302, and to the Office of Information and Regulatory Affairs, Office of Management and Budget, Washington, DC 20503.</p>			
<b>1. AGENCY USE ONLY (Leave blank)</b>	<b>2. REPORT DATE</b> June 2004	<b>3. REPORT TYPE AND DATES COVERED</b> Technical Report	
<b>4. TITLE AND SUBTITLE</b> Electric Field Floats in the North Atlantic Current: Validation and Observations			<b>5. FUNDING NUMBERS</b> APL-UW administered no funds to produce this work.
<b>6. AUTHOR(S)</b> Zoltan B. Szuts			
<b>7. PERFORMING ORGANIZATION NAME(S) AND ADDRESS(ES)</b> Applied Physics Laboratory University of Washington 1013 NE 40th Street Seattle, WA 98105-6698			<b>8. PERFORMING ORGANIZATION REPORT NUMBER</b>
<b>9. SPONSORING / MONITORING AGENCY NAME(S) AND ADDRESS(ES)</b>			<b>10. SPONSORING / MONITORING AGENCY REPORT NUMBER</b>
<b>11. SUPPLEMENTARY NOTES</b>			
<b>12a. DISTRIBUTION / AVAILABILITY STATEMENT</b> Approved for public release; distribution is unlimited.			<b>12b. DISTRIBUTION CODE</b>
<b>13. ABSTRACT</b> (Maximum 200 words) <p>Electric field floats were designed and built to measure depth-averaged velocity. They were made from commercial RAFOS floats modified to make horizontal electric field measurements through the addition of two pairs of electrodes, electrode arms, rotation vanes, a compass, amplifiers, and a microprocessor. The added second system coordinated its activities with the RAFOS system by an optical serial connection. The electric field observations were combined with RAFOS-derived velocities to form conductivity-weighted depth-averaged velocities, which are close to the depth-averaged or barotropic velocity. Two factors relate the former to the latter: baroclinic covariance in the vertical between electrical conductivity and velocity, and the ratio of bottom sediment electrical conductance to water column conductance. These were calculated and applied to obtain barotropic velocity.</p> <p>Four electric field floats were deployed in the North Atlantic Current in the fall of 1994. They were launched in an eastward flowing branch of the current and were carried through numerous eddies during their 40-day deployments. Hydrographic data collected after deployment permits validation of the electromagnetic method and estimation of the factors relating conductivity-weighted depth-averaged velocities to barotropic velocity.</p> <p>This report is a slightly modified version of the thesis submitted in partial fulfillment of the requirements for the degree of Master of Science at the University of Washington. Dr. Thomas Sanford was the chair of the supervisory committee.</p>			
<b>14. SUBJECT TERMS</b> North Atlantic Current, electrical field floats, RAFOS			<b>15. NUMBER OF PAGES</b> 86
			<b>16. PRICE CODE</b>
<b>17. SECURITY CLASSIFICATION OF REPORT</b> Unclassified	<b>18. SECURITY CLASSIFICATION OF THIS PAGE</b> Unclassified	<b>19. SECURITY CLASSIFICATION OF ABSTRACT</b> Unclassified	<b>20. LIMITATION OF ABSTRACT</b> SAR